The role of SnO_2 in the bifunctional mechanism of CO oxidation at Pt-SnO_2 electrocatalysts

Haoliang Huang[a], Edward T.C. Hayes[a], Diego Gianolio[b], Giannantonio Cibin[b], Fredrik S. Hage[c], [d], Quentin M. Ramasse[c], [e] and Andrea E. Russell*[a]

[a] Dr. H. Huang, Mr. E.T.C. Hayes, Prof. A.E. Russell
School of Chemistry, University of Southampton, Highfield, Southampton SO17 1BJ, United Kingdom
E-mail: a.e.russell@soton.ac.uk
[b] Dr. D. Gianolio and Dr. G. Cibin
Diamond Light Source Ltd, Diamond House, Harwell Campus, Didcot OX11 0DE, United Kingdom
[c] Dr. F.S. Hage and Prof. Q.M. Ramasse
SuperSTEM Laboratory, SciTech Daresbury Campus, Daresbury WA4 4AD, United Kingdom
[d] Dr. F.S. Hage
Department of Physics / Centre for Materials Science and Nanotechnology, University of Oslo, NO-0318 Oslo, Norway
[e] Prof. Q.M. Ramasse
School of Physics and Astronomy and School of Chemical and Process Engineering, University of Leeds, Leeds LS2 9JT, United Kingdom

Supporting information for this article is given via a link at the end of the document.

Abstract: Pt-Sn bimetallic catalysts, especially Pt-Sn alloys, are considered highly CO-tolerant and are thus candidates for reformate derived hydrogen oxidation and for direct oxidation of fuel cell molecules. However, it remains unclear if this CO-tolerance originates from Sn in the Pt-Sn alloy or whether SnO_2, present as a separate phase, also contributes. In this work, a carbon-supported Pt-SnO_2 was carefully synthesized to avoid the formation of Pt-Sn alloy phases. The resulting structure was analysed by scanning transmission electron microscopy (STEM) and detailed X-ray absorption spectroscopy (XAS). CO oxidation voltammograms of the Pt-SnO_2/C and other SnO_2-modified Pt surfaces unambiguously suggest that a bifunctional mechanism is indeed operative at such Pt-SnO_2 catalysts for stable CO oxidation at low overpotentials. The results from these studies suggest that the bifunctional mechanism can be attributed to the co-catalysis role of SnO_2, in which the surface hydroxide of SnO_2 (Sn-OH) reacts with CO adsorbed on Pt surface (Pt-CO_{ads}) and regenerates via a Sn^{II}/Sn^{IV} reversible redox couple (-0.2–0.3 V *vs.* reversible hydrogen electrode).

Introduction

Carbon monoxide oxidation remains an important reaction in proton-exchange membrane (PEM) fuel cells, as CO is present as an impurity from reformate gas[1] and is also an intermediate or incomplete oxidation product of small fuel molecules (methanol, ethanol, etc.)[2]. CO poisons Pt surfaces and thus severely retards the oxidation of fuel molecules[3]. Amongst CO-tolerant catalysts, Pt-Sn alloys stand out[4], due to a combination of the following promotional effects: (i) bifunctional effects, through which the Sn sites provide the adsorbed hydroxide (OH_{ads}) reactant at much lower potential than at Pt[5]; (ii) electronic/ligand effects, through which alloyed Sn atoms alter the electronic properties of Pt and thus weaken the Pt-CO interaction[4d, 6]; and (iii) ensemble effects, through which the binding site geometry of CO on Pt is altered because the Pt surface is diluted by CO-inert but hydrophilic Sn atoms[6]. Nevertheless, for practical applications, the instability of the active Pt-Sn alloy surfaces and Sn dissolution narrow the useful upper limit of the potential window to 0.5~0.6 V (*vs.* the standard hydrogen electrode, which will be used as the reference for all potentials referred to in the introduction) in acidic electrolytes[7]. Additionally, the ensemble effects of surface-alloyed Sn have been shown to inhibit C-H bond dissociation in methanol oxidation[8] and to lower the CO_2 selectivity in ethanol oxidation[2a, 8a, 9].

Pt modified SnO_2, Pt-SnO_2, in which the contributions from the ligand and ensemble effects no longer exist, has been shown to promote the oxidation of CO and other site-blocking intermediates via a bifunctional mechanism similar to that for the Pt-Sn alloy [4b, 10]. Our group[11] reported a study of well-characterized Pt-Sn nanoparticles, in which the SnO_2-to-alloyed Sn ratio was changed by heat treatment in different atmospheres. We found that whilst the onset potential of CO stripping increased, it was not proportional to the fraction of SnO_2 (~0.39 V for the sample with ~92 at % SnO_2 out of total Sn), implying that both SnO_2 and alloyed Sn may facilitate CO oxidation on Pt[11]. This relationship is supported by other studies on Pt-Sn bimetallic catalysts[12], and the promoted CO oxidation can be also found on Sn modified Pt nanoparticles, in which the Sn was suggested to exist as SnO_2[9b, 13]. In addition, the surfaces of Pt-Sn alloys tend to segregate into Pt-Sn^{4+} or Pt-SnO_2 due to the instability to air exposure[14], as observed during low-temperature CO oxidation [15], suggesting that the bifunctional effects reported on Pt-Sn bimetallic catalysts may be partly attributed to SnO_2.

If a bifunctional mechanism is active for Pt-SnO_2 catalysts, a redox couple corresponding to the formation and dissociation of Sn-OH should exist, as Hayden *et al.*[5a] found on Pt(111)/Sn surface alloys. Cathro[16] proposed that increased activity of a Pt-Sn catalyst, electrodeposited from a mixed solution of H_2PtCl_6 and $SnCl_4$ at 0.05 V, for the oxidation of C_1 fuel molecules oxidation could be ascribed to the $Sn(OH)_3^+/Sn^{2+}$ couple (0.142 V[17]). On the other hand, Rabis *et al.*[18] showed two irreversible redox couples on a SnO_2 thin film, the presence of which depends on the (reducing or oxidising) synthesis conditions; SnO_2 prepared under reducing conditions at ~0.1 V/~0.4 V and that prepared under oxidising conditions at ~-0.2 V/~-0.3 V. Lim *et al.*[19] reported an irreversible redox couple at ~0.7 V/~0.5 V of partially alloyed PtSn and attributed this to the absorption and desorption of oxygen-containing species of SnO_2. Matsui *et al.*[20] observed a similar redox couple on a SnO_x supported Pt catalyst.

Although bifunctional effects from SnO_2 are likely to exist and have comparable enhancement for CO oxidation to that of the alloys, unambiguous evidence of the bifunctional effects is still lacking. To ascertain the contribution of the bifunctional mechanism from SnO_2, a catalyst Pt-SnO_2 in which no Pt-Sn alloying is present is required. The study reported herein has been carefully designed to achieve such a catalyst to enable unambiguous exploration of the contributions of SnO_2 to the bifunctional mechanism.

To obtain such an unalloyed Pt-SnO_2 catalyst, the choice of Sn precursors and the reducing condition need to be taken into careful consideration to avoid the formation of the strong Pt-Sn intermetallic bond whilst increasing the number of Pt-SnO_2 interfaces. First, the commonly used stannous chloride ($SnCl_2$) should be avoided, because the oxidation state of Sn is not the targeted one, and more importantly because $SnCl_2$ can form a Pt-$SnCl_3$ complex with Pt precursors[21]. Secondly, the reducing agent should be of modest strength, so as to selectively reduce only the Pt ions and should not contain organic residues that complicate the interpretation of results. Considering these two factors, sodium stannate (Na_2SnO_3) and stannic chloride ($SnCl_4$) could be good choices for the Sn precursor, and room-temperature reduction in a H_2(g) atmosphere could reduce Pt (hydro)oxides (PtO_x) to metallic Pt whilst leaving the SnO_2 unaltered, based on the differences between the standard electrode potentials of Pt, Sn, and H, in which the reducing potential of H_2/H^+ (0 V) is much lower than that of $Pt^{II}O$ /Pt or $Pt^{IV}O_2$/Pt (both ~1.0 V) but higher than that of SnO_2/Sn^0 (both ~-0.1 V) [17]. Room temperature reduction is also used to prevent intermixing Sn and Pt atoms, as heat treatment (≥200 °C) is required for the formation of Pt-Sn alloy nanoparticles [11, 22].

In this work, a Pt-SnO_2 nanoparticle catalyst supported on carbon (Pt-SnO_2/C) is synthesised based on the above considerations. The distribution of Pt and SnO_2 and the morphology are studied by analytical electron microscopic techniques and the Sn speciation is interrogated by detailed X-ray absorption spectroscopy analysis. On Pt-SnO_2/C, CO oxidation at low overpotentials is promoted and capable of proceeding without being poisoned, supporting our hypothesis that bifunctional effects from SnO_2 are active in CO oxidation. The bifunctional mechanism of SnO_2 is also supported by mixtures of commercial Pt/C and SnO_2 nanoparticles and is further studied by depositing SnO_2 nanoparticles on Pt disc electrodes and carbon electrodes.

Results and Discussion

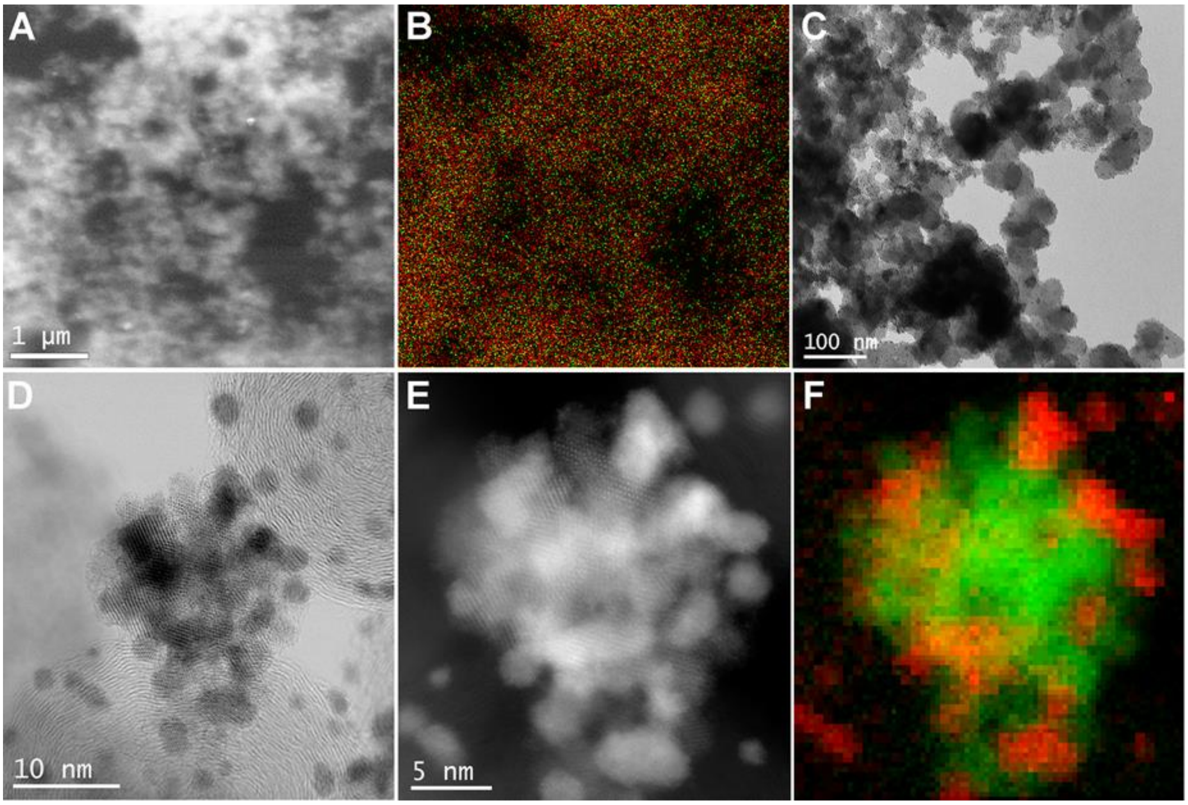

Figure 1. Elemental distribution and morphology of Pt-SnO_2/C. (A) A SEM image and (B) the corresponding EDS mapping image of Pt $M_{\alpha 1}$ (red) and Sn $L_{\alpha 1}$ (green). (C) An overview TEM image, (D) BF and (E) HAADF STEM images zooming in on a mixed Pt-SnO_2 region, and (F) the corresponding STEM-EELS composite map, using Pt $M_{4,5}$ edge (red), and overlapping Sn $M_{4,5}$ and O K edges (green). The SEM sample was drop-casted as a thin film on a carbon-coated Cu grid.

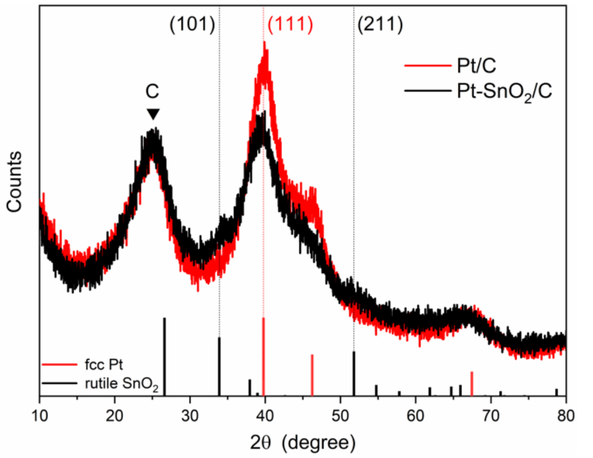

Figure 2. XRD patterns of Pt-SnO$_2$/C and Pt/C powder samples, along with the standard patterns of fcc Pt (JCPDS No. 04-0802) and rutile SnO$_2$ (JCPDS No. 41-1445). The peak ascribed to the carbon support is indicated. The Pt loading of Pt/C is ~12.6 wt%, and the Pt and SnO$_2$ loadings of Pt-SnO$_2$/C are ~12.3 wt% and 4.0 wt%, respectively.

The elemental distribution and morphology of the as-prepared samples were studied using analytical electron microscopic techniques. **Figure 1** shows a SEM secondary electron (SE) image (**Figure 1A**) and corresponding EDS map of a Pt-SnO$_2$/C sample (**Figure 1B**). The sample was deposited as a thin film on a carbon-coated Cu grid to minimize particle stacking. At this large field of view (~ 5 μm), the Sn and Pt signal appear to co-locate, suggesting that, on the whole, SnO$_2$ in Pt-SnO$_2$/C distributes evenly, rather than forming large-scale agglomerates and separating from Pt and carbon. **Figures 1C-D** show representative bright field (BF) (S)TEM images of Pt-SnO$_2$/C with fields of view ~600 nm and ~40 nm, respectively, displaying that the nanoparticles are uniformly deposited on the carbon support in the form of isolated nanoparticles (~1.9 nm, **Figure S3**) and nanoparticle clusters (~10 nm). The well-dispersed and isolated nanoparticles are found to be pure Pt, i.e., with no detectable Sn or O STEM electron energy loss spectroscopy (EELS) signal (**Figure S4** and **Figure S5**). These isolated Pt particles dominate in the as-prepared Pt/C (**Figure S6**). Close-up BF and high angle annular dark field (HAADF) STEM images (**Figure 1D-E, Figure S7A-B** for another region) reveal that the nanoparticle clusters of Pt-SnO$_2$/C are assemblies of nanocrystals. STEM-EELS results, see both elemental maps (**Figure 1F, S7C, S8B**) and EEL spectra from selected regions (**Figure S8C-E),** suggest that the nanoparticle clusters consist of Pt and tin oxide nanoparticles with comparable particle sizes, and that these two types of particles are in intimate contact.

Crystalline phases of the as-prepared samples were also identified using powder X-ray diffraction (XRD). **Figure 2** shows XRD patterns of Pt-SnO$_2$/C and Pt/C, along with standard peak positions of face-centred cubic (fcc) Pt and rutile SnO$_2$ as vertical bars in the diagram. Pt-SnO$_2$/C largely shares a pattern with Pt/C, with a broad diffraction peak (~25°) from Vulcan XC-72R carbon (**Figure S11**) and a set of peaks (~40°, 46° and ~67°) from fcc Pt. The only mismatches found on Pt-SnO$_2$/C are the weak yet discernible peaks at ~34° and ~52°, which can be indexed to SnO$_2$(101) and SnO$_2$(211), respectively. The SnO$_2$ diffraction peaks are also observed in the precursor of Pt-SnO$_2$/C before H$_2$ reduction (**Figure S11A**), and they become more dominant and more defined when the SnO$_2$ loading is increased (**Figure S11B**). Thus, the weak signal of the SnO$_2$ phase in Pt-SnO$_2$/C is possibly due to the nanocrystalline nature of the SnO$_2$ and the low concentration of SnO$_2$ (~4 wt%). Other than those from Pt, SnO$_2$ and carbon, no extra diffraction peaks relating to crystalline Pt$_3$Sn phases or other Pt-Sn alloys are observed, indicating that the crystalline Sn of Pt-SnO$_2$/C is in the form of SnO$_2$ rather than alloyed Sn. In addition, from the width of the Pt (111) diffraction peak, average Pt crystallite sizes of Pt-SnO$_2$/C and Pt/C were estimated to be ~1.8 nm and ~2.1 nm, respectively, which are in agreement with the particle size measured from the corresponding TEM images.

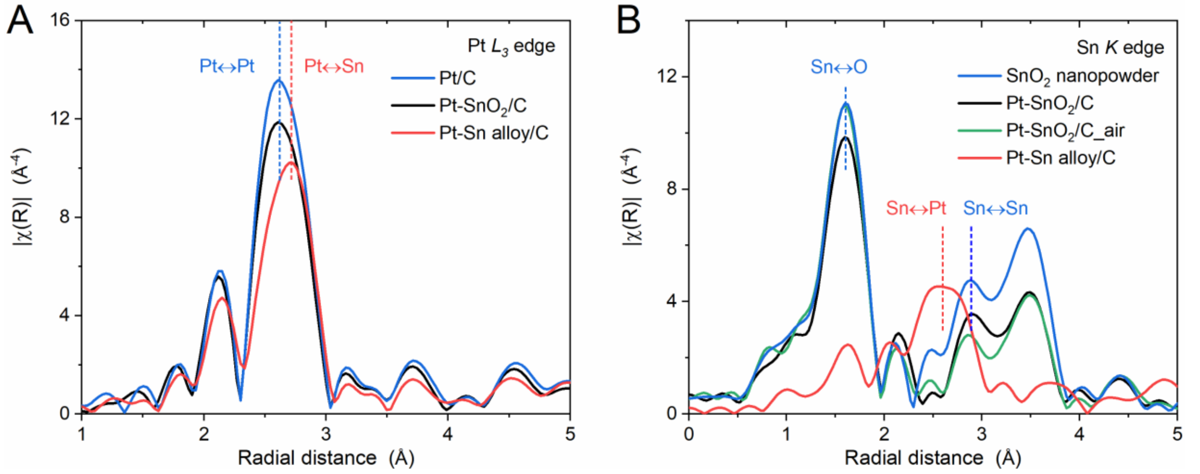

Figure 3. Fourier transforms without phase correction of k^3-weighted EXAFS spectra of Pt-SnO$_2$/C at (A) Pt L_3 edge and (B) Sn K edge, compared to those of the reference samples, Pt/C at Pt L_3 edge, SnO$_2$ nanopowder at Sn K edge and Pt-Sn alloy/C at both edges. The comparison is also shown in both k space and the real part of R space (**Figure S12** for the Pt edge data and **Figure S13** for the Sn edge data). The samples were measured as BN pellets and in H$_2$(g), except for the SnO$_2$ nanopowder and one of Pt-SnO$_2$/C samples, which were measured in air.

Table 1. Structural parameters of Pt-SnO_2/C, Pt-SnO_2/C_air (Pt-SnO_2/C measured in air), Pt-Sn alloy/C, Pt/C, SnO_2 nanopowder, and Pt foil, obtained from EXAFS fitting. Double dataset fitting was conducted on Pt-Sn alloy/C[e].

Sample	Edge [a]	Scattering path*	*R* (Å) [b]	*N* [c]	σ^2 (x10^3 Å^2) [d]	ΔE_0 (eV)	R factor (%)
Pt-SnO_2/C	Pt L_3	Pt–Pt	2.754(2)	8.8(3)	6.5(2)	5.6(4)	0.68
	Sn *K*	Sn–O	2.054(7)	5.6(3)	4.3(8)	5(1)	1.2
		Sn–Sn	3.21(2)	2(1)	7(3)		
Pt-SnO_2/C_air	Sn *K*	Sn–O	2.052(4)	6.1(2)	4.2(5)	4.2(6)	0.4
		Sn–Sn	3.21(1)	1.6(7)	6(2)		
Pt-Sn alloy/C	Pt L_3	Pt–Pt	2.779(1)	8.2(2)	6.9(1)	4.9(2)	0.88
		Pt–Sn	2.788(5) [e]	2.2(2)	12(1) [e]		
	Sn *K*	Sn–O	2.02(3)	1(1)	4(8)	3(1)	
		Sn–Pt	2.788(5) [e]	9(2)	12(1) [e]		
Pt/C	Pt L_3	Pt–Pt	2.756(2)	9.3(3)	6.2(2)	6.8(3)	0.57
SnO_2	Sn *K*	Sn–O	2.055(4)	6.0(2)	4.0(5)	4.2(6)	0.33
		Sn–Sn	3.201(7)	1.2(5)	2(2)		
Pt foil [f]	Pt L_3	Pt–Pt	2.765(1)	12	4.9(1)	7.2(3)	1.6

[a] For the Pt L_3 edge data, only the first coordination shell is presented;

[b] *R*, the average distance of absorber–backscatterer pair scattering; [c] *N*, the coordination number of the scattering; [d] σ^2, the mean square relative displacement of the *R*.

[e] For Pt-Sn alloy/C data, Pt–Sn and Pt–Sn scatterings were constrained to have an equal R and σ^2;

[f] The coordination numbers of different shells were kept the same as the theoretical model (ICSD No. 52250).

Although only SnO_2 and no crystalline Pt-Sn alloy could be found by XRD, this evidence alone is insufficient to assert that no Pt-Sn alloy phase exists in Pt-SnO_2/C. If there were alloyed Sn species, they might be oxidized after exposure to air[14], and/or at concentrations below the detection limit of XRD. Thus, the Sn speciation of Pt-SnO_2/C was further characterised from aspects of local coordination environment and oxidation state and by combining XAS spectra obtained at the Pt L_3 and Sn *K* edges. The spectra were collected in H_2(g) to mimic the synthesis condition, which minimises the air-induced oxidation and dealloying of potential Pt-Sn alloy phases.

At the Pt L_3 edge, Pt-SnO_2/C shows a Fourier-transformed (FT) extended X-ray absorption fine structure (EXAFS) spectrum matching that of Pt/C but with slightly decreased magnitude (**Figure 3A**), which is also reflected in the *k* space and the real part of the *R* space plots (**Figure S12**), suggesting similarity in the Pt coordination environment. Quantitative results of Pt coordination were found from the corresponding multiple-shell fitting using a constrained model, where the symmetry of Pt fcc structure is used to minimise the number of variables. The fits of both Pt-SnO_2/C and Pt/C yield good R-factors (<0.7%), with Pt–Pt distances (*R*) within the error of fitting, 2.754(2) Å *vs.* 2.756(2) Å, respectively (**Figure S14** and **Table 1**). As the fitted values for the mean square relative displacement (σ^2) are also similar, the decreased FT magnitude for the Pt-SnO_2 is attributed to the lower coordination number (CN) of Pt–Pt (~8.8 for the first-shell) than Pt/C (~9.3), which is consistent with the smaller Pt particle size of Pt-SnO_2/C indicated by TEM and XRD. In contrast, the Pt-Sn alloy/C data show a Pt–Sn scattering path, *R* (~2.79 Å) (**Figure 3A**), due to the alloying of Sn atoms[9b, 11] and a Pt–Pt distance (~2.779 Å) which is significantly longer than that of Pt/C (~2.756 Å, **Figure S15** and **Table 1**).

The contrasting Sn speciation of Pt-SnO_2/C and Pt-Sn alloy/C can be more readily distinguished from the perspective of Sn. At the Sn *K* edge, the FT of the EXAFS for the Pt-SnO_2/C shows a similar profile to that for the SnO_2 nanopowder (**Figure 3B** and **Figure S13**), whilst that for the alloy sample is dominated by a unique Sn–Pt scattering path (~2.79 Å, **Figure S15** and **Table 1**), which cannot be detected or fitted for the Pt-SnO_2/C data (**Figure S16**). Further examination reveals that the FT magnitude of Pt-SnO_2/C is lower than that of the SnO_2 in two regions, the Sn–O region (1.0–2.0 Å) and the high *R* region (2.5–3.8 Å). The lower magnitude in the former region yields a CN of 5.6(3), less than the theoretical value of SnO_2 (CN = 6, **Figure S17**), which indicates that the SnO_2 of Pt-SnO_2/C is unexpectedly reduced to a limited extent. To clarify the origin of the reduced SnO_2, Pt-SnO_2/C was also measured in air. A good match with SnO_2 nanopowder is shown in the Sn–O region (**Figure 3B**), with the fit yielding a CN of 6.1(2), suggesting that the SnO_2 in the as-prepared Pt-SnO_2/C is fully oxidized with a SnO_6 first shell coordination. For the high *R* region, the decreased FT magnitude of Pt-SnO_2/C (measured in air and in H_2) is attributed to the crystallite size of SnO_2. Sn–Sn scattering paths between neighbouring SnO_6 units dominate in this region, and such a decrease is also observed when the SnO_2

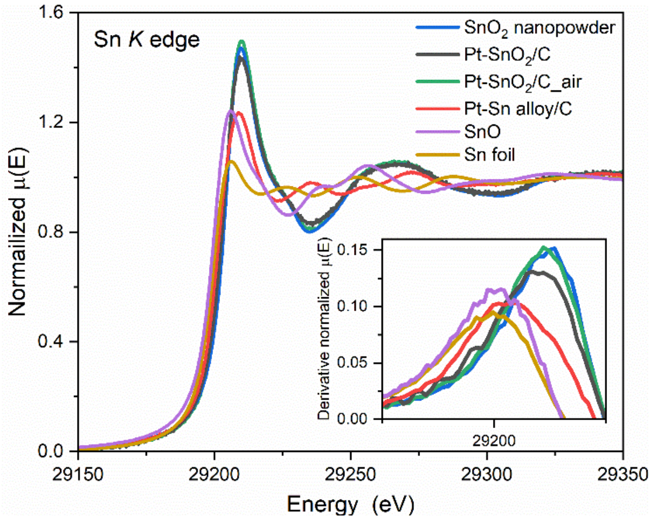

Figure 4. Sn *K* edge XANES spectra and (the inset) their first derivatives of Pt-SnO_2/C and the reference samples SnO_2 nanopowder, SnO, Pt-Sn alloy/C and Sn foil. The spectra of Pt-SnO_2/C, Pt/C and Pt-Sn alloy/C were collected in H_2(g), and the others in air.

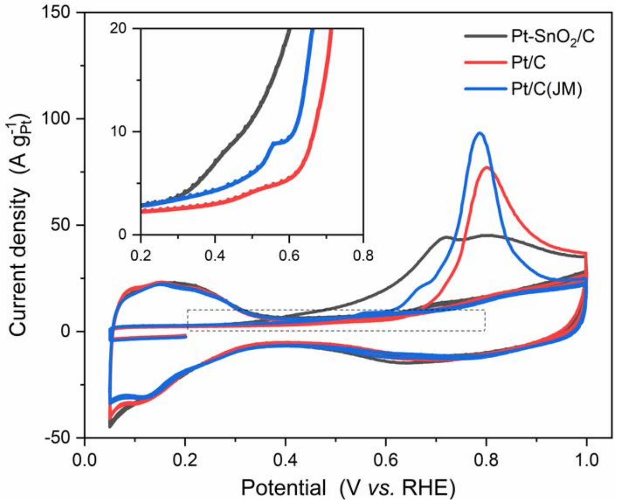

Figure 5. CO stripping voltammograms of Pt-SnO_2/C, Pt/C and Pt/C (Johnson Matthey) in N_2-saturated 0.1 M $HClO_4$ solution at a scan rate of 20 mV s^{-1}. A saturated CO adlayer was adsorbed by potential hold at 0.2 V for at least 15 min, followed by displacement of dissolved CO from the solution by N_2.

nanopowder (8–10 nm) is compared with a SnO_2 standard sample (**Figure S18**). The small crystallite size of SnO_2 in Pt-SnO_2/C is consistent with the nanocrystalline nature observed by STEM (~2–3 nm). Thus, the mismatches between Pt-SnO_2/C and SnO_2 in the Sn *K* edge EXAFS spectra originate from a combination of the measurement atmosphere and the size of the SnO_2 particles, rather than the presence of alloyed Sn in the as-prepared Pt-SnO_2/C.

The dominance of SnO_2 in the Sn speciation of Pt-SnO_2/C is corroborated by X-ray absorption near-edge structure (XANES) spectra at Sn *K* edge (**Figure 4)**. Compared to Sn references (SnO_2 nanopowder, Pt-Sn alloy/C, SnO and Sn foil), Pt-SnO_2/C samples, measured in air and in H_2(g), show a nearly identical spectrum to that of the SnO_2 in terms of white line intensity (the sharp feature at the top of the rising edge), peak position (selected as the maximum of the first derivative, the inset of **Figure 4**) and other fine structures above the edge (29250–29400 eV), consistent with the EXAFS results. The concentration of each possible Sn species in the as-prepared Pt-SnO_2/C (measured in air) was estimated by linear combination fitting (LCF) using two components, SnO_2 and the other Sn references. The fitting suggests that the Sn species of the Pt-SnO_2/C are comprised of 100% SnO_2. We note for completeness that X-ray absorption spectroscopy (XAS) is unable to exclude the presence of trace amounts of alloyed Sn in the sample. STEM-EELS microanalysis of one region (see **Figure S9**, **Figure S10** and the related discussion in the supporting information) shows that Sn, most likely in the form of bulk alloyed Sn, was present in Pt particles in contact with SnO_2, the exact origin of which is unclear. Thus, based on the differences between SnO_2 and alloyed Sn in XANES and the nearly identical spectra of Pt-SnO_2/C and SnO_2, we estimate that >99.9 % Sn atoms exist as SnO_2 in the as-prepared Pt-SnO_2/C.

Further inspection of the Pt-SnO_2/C XANES spectra reveals a slight reduction of the SnO_2 when the spectra were measured in H_2(g), consistent with the EXAFS data, and LCF yields (99.1 ± 1.5)% SnO_2 and (0.9 ± 1.5)% reduced SnO_2, using Pt-Sn alloy/C as the component of the reduced species (**Figure S19**). The possible speciation of the reduced SnO_2 is then discussed. Careful comparison of the FT EXAFS spectra measured in H_2(g) and air (**Figure 3B** and **Figure S13**) reveals a small yet discernible mismatch in position at a radial distance of ~2.3 Å, which would suggest a new scattering path. Such a mismatch is supported in the fit of Pt-SnO_2/C (**Figure S16**), in which the scattering paths were generated using rutile SnO_2 (ICSD No.647469) as the input file, present as a peak at ~2.2 Å in the residual plot (**Figure S20**). However, the mismatch at ~2.3 Å and the residual peak at ~2.2 Å cannot be attributed to the formation of new phases, as the common Sn references like alloyed Sn and SnO show no major scattering path in these two regions (**Figure S20** and **Figure S21**). We therefore suggest, as the most likely explanation, that the reduced SnO_2 arises from surface oxygen vacancies on SnO_2, in which oxygen-containing ligands were partly depleted by H_2. This suggestion is consistent with the surface composition and structure of SnO_2: low index SnO_2 surfaces under reducing conditions tend to lose surface lattice oxygen and relax into a Sn^{II} state termination[23]. One may notice that this surface Sn^{II} can be easily oxidised under ambient conditions, as shown in the XAS data measured in air. This dual valency gives us the first indication that a redox couple may exist on the SnO_2 surface.

Figure 5 shows the CO-stripping voltammograms of the as-prepared samples, Pt-SnO_2/C and Pt/C, as well as a commercial Pt/C (20 wt%) (Johnson Matthey (JM)). After a saturated CO adlayer was formed at 0.2 V in 0.1 M $HClO_4$, the potential was swept backwards to 0.05 V in CO-free electrolyte and cycled from 0.05 – 1.0 V for three cycles. The hydrogen adsorption/desorption ($H_{ads/des}$) features from Pt (0.05 – 0.35 V) are absent in the first cycle, as the Pt surface is completely blocked by the adsorbed CO (CO_{ads}) and appear in the 2nd and 3rd cycles when the CO_{ads} is stripped off. The $H_{ads/des}$ pseudocapacitive current of Pt-SnO_2/C largely overlaps that of the Pt/C catalysts with comparable charge, whilst those of Pt-Sn alloy/C are considerably smaller (**Figure S22** and **Table S1**).

For the 1st CO stripping sweeps, whilst the Pt/C catalysts show a main peak at ~0.8 V and small pre-peaks between 0.4 V and 0.7 V (the inset of **Figure 5**), and compared to the prepared Pt/C the larger contribution of the pre-peak and the earlier onset of CO stripping observed for the commercial Pt/C can be attributed to the agglomeration of Pt particles and the larger particle size (**Figure S6 and Figure S23**)[24]. In contrast to the Pt/C catalysts, Pt-SnO_2/C gives a broad peak, from 0.3 V to 1 V, with significantly more contribution from the pre-peaks and less from the main peak. Two CO stripping features of Pt-SnO_2/C are noteworthy. The first is the low onset potential (~0.3 V), which is close to the reported value for Pt-Sn alloys[5a, 6a] and Sn-modified Pt[25], indicating that CO oxidation at the Pt-SnO_2 catalyst is indeed promoted. The second is the broad peak shape, suggesting that highly active and less active sites (pure Pt sites) coexist on Pt-SnO_2/C. The multiplicity of active sites is consistent with the STEM results revealing that some Pt particles are isolated from SnO_2. The percentage of highly active sites can be estimated by a CO pre-stripping voltammogram (**Figure S24**), in which ~36% CO_{ads} was removed by potential hold at 0.5 V prior to CO stripping.

The CO stripping voltammogram features of Pt-SnO_2/C are reproducible in sulfuric acid electrolyte (**Figure S25**), and for catalysts comprising physical mixtures of two commercial components, Pt/C (60 wt%, JM) and SnO_2 nanopowders (8–10 nm), prepared over a range of molar ratios of Pt to SnO_2 (3:1, 1:1 and 1:3, **Figure 6A**). A consistent trend is clearly obtained; increased SnO_2 loading is accompanied by a greater change to the pre-peak region. As a control the promoted SnO_2 was replaced by Al_2O_3, resulting in no promotion of the CO oxidation (**Figure S26**). The charge in the pre-peak region decreases significantly when the configuration of thin-film electrodes was changed from physical mixtures to layer-by-layer structures (a SnO_2 layer on a Pt/C layer and *vice versa*), suggesting that the promotion effects from SnO_2 depend not simply on the presence or content of SnO_2, but also on the contact between Pt and SnO_2 (**Figure 6B**).

Since SnO_2 itself is inert for CO oxidation (**Figure S27**), the CO stripping voltammograms of the Pt-SnO_2/C and the physical mixtures of Pt/C and SnO_2 clearly indicate that CO adlayer oxidation at the Pt surface is facilitated by $Sn^{IV}O_2$. The conventional bifunctional mechanism from alloyed Sn, in which water molecules are activated by the oxidation of the Sn sites[5a, 6a], fails to explain the promotional effect from SnO_2. One may argue that the mechanism is still applicable at SnO_2 by forming OH_{ads} adsorbed on SnO_2, as hypothesised by many previous studies[10, 19a, 26]. We argue otherwise that it is the OH species on the SnO_2 surface, (SnO_2)Sn-OH, that are the active species for the bifunctional mechanism from SnO_2. Our reasons are twofold. First, Sn^{IV} of SnO_2 is in the highest oxidation state of Sn and has a saturated first coordination shell, as ascertained by XAS above. These two factors do not allow the addition of OH coordination by further oxidation of Sn^{IV}. Second, the presence of surface hydroxyl species on SnO_2 has been previously verified and found to be formed by the absorption and dissociation of water [23, 27]. In heterogeneous catalysis the surface hydroxyl on SnO_2 has been found to participate in CO oxidation on Pt at low temperature[28]. Thus, based on the widely accepted Langmuir-Hinshelwood (L-H) type reaction of CO oxidation on Pt[2d, 4a, 29], the bifunctional mechanism from SnO_2 can be tentatively written as

$$\text{Pt-CO}_{ads} + (SnO_2)\text{Sn-OH} + H_2O \rightarrow CO_2 + H_3O^+ + e^- + \text{Pt} + (SnO_2)\text{Sn}^* \qquad \text{(eq. 1)}$$

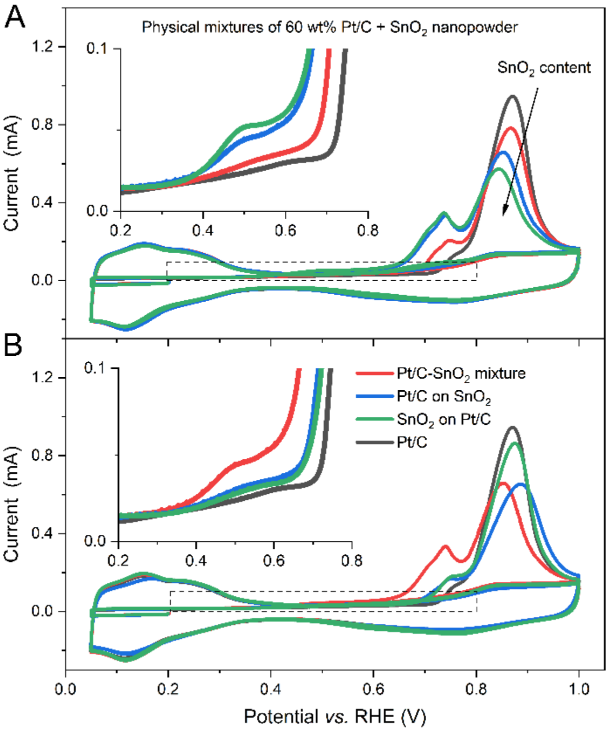

Figure 6. CO stripping voltammograms of electrodes modified by 60 wt% Pt/C (Johnson Matthey) and SnO_2 nanopowder with different (A) SnO_2 contents and (B) microstructures. (A) Physical mixtures of the Pt/C and the SnO_2 (Pt:Sn molar ratios of 3:1, 1:1 and 1:3), with a constant Pt loading on the electrodes (~61 μg_{Pt} cm^{-2}) and with the SnO_2 loadings of 0 μg cm^{-2} (black), ~15 μg cm^{-2} (red), ~46 μg cm^{-2} (blue) and ~138 μg cm^{-2} (green). Arrow shows increasing SnO_2 loading. (B) Layer-on-layer structures formed via drop-casting sequences (a Pt/C layer on a SnO_2 layer, and *vice versa*), keeping the Pt and SnO_2 loading constant, ~61 μg cm^{-2} and ~46 μg cm^{-2}, respectively. The voltammograms were conducted in N_2-saturated 0.1 M $HClO_4$ solution with a scan rate of 20 mV s^{-1}, and the insets magnify the first sweeps of the voltammograms at the onset of CO_{ads} oxidation.

where (SnO_2)Sn* represents surface oxygen vacancy sites of SnO_2, possibly as the reduced SnO_2 measured by XAS in H_2(g), and thus the reaction rate is the product of a rate constant and the coverage of Pt-CO_{ads} and (SnO_2)Sn-OH at Pt-SnO_2 interfaces. However, the surface defect site of SnO_2 may or may not form back to Sn-OH under the experimental conditions. If not, or with slow kinetics, the Sn-OH would be consumed, and the reaction would be discontinued.

To further investigate the regeneration of the Sn-OH species, CO oxidation at Pt-SnO_2 was studied by CO continuous oxidation voltammetry. The measurements were carried out in a CO-saturated electrolyte, and the mass transport of the dissolved CO was controlled by rotating disc electrode (RDE) configuration, so that the CO_{ads} coverage is kept constant. The upper limits of the potential windows were chosen to emphasise the pre-peak characteristic, i.e., 0.6 V for Pt-SnO_2/C and 0.7 V for the Pt/C catalysts.

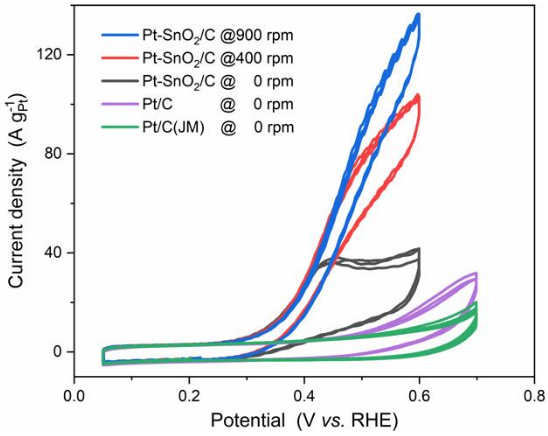

Figure 7. CO continuous (dissolved) oxidation voltammograms of Pt-SnO_2/C, Pt/C and Pt/C (Johnson Matthey) in CO-saturated 0.1 M $HClO_4$ solution with a scan rate of 20 mV s^{-1}. The rotation rates are indicated in the figure legend. The CO oxidation currents of the Pt/C catalysts show no enhancement with rotation rate (**Figure S28**).

Figure 7 shows the CO continuous oxidation voltammograms of Pt-SnO_2/C, Pt/C and commercial Pt/C. As Pt surface sites are continuously blocked by CO_{ads} in CO-saturated electrolyte, the voltammograms show no $H_{ads/des}$ features in all three cycles. Compared to the 1st sweep of CO stripping voltammograms, the CO oxidation currents are enhanced with the continuous supply of CO, but the extent of enhancement varies with the catalyst (**Figure S28**). Pt-SnO_2/C shows the most enhancement under stationary conditions, especially at the onset of CO oxidation, and the current can be further enhanced by increasing the rotation rate (**Figure 7**), which is not observed on the Pt/C catalysts even when the upper limit of the potential windows were extended to 0.9 V (**Figure S29** and **Figure S30**). The rotation rate-dependent current indicates that the CO oxidation kinetics on Pt-SnO_2/C are so fast that the diffusion of dissolved CO becomes the rate-determining step when the potential is ≥ 0.4 V. Such fast kinetics at such a low potential have rarely been reported. Gasteiger *et al.*[1a] reported similar rotation rate-dependent CO oxidation current on a well-characterised Pt_3Sn electrode but over a narrower potential windows (< 0.5 V) to avoid Sn dissolution.

From the kinetically controlled portion of the voltammogram, a constant Tafel slope of ~134 mV dec^{-1} was obtained for the low potential CO oxidation (over 6–50 A g_{Pt}^{-1}, **Figure S31**). The value is similar to those in two previously reports, one for the pre-peak CO oxidation on Pt(111) in an alkaline electrolyte (130 mV dec^{-1})[30] and another simulated on Pt in an acidic electrolyte when OH coverage is saturated and potential-independent (120 mV dec^{-1})[31]. Both cases consider the L-H reaction between Pt-CO_{ads} and OH_{ads} to be the rate-determining step of CO oxidation.

In addition to the enhanced current, no shift is observed in the CO continuous oxidation voltammograms for Pt-SnO_2/C during the sequence of successive cycles at different rotation rates (**Figure 7** and **Figure S28)**, compared to a continuous positive shift observed for the Pt/C catalyst (**Figure S29** and **Figure S30**). The deactivation of Pt/C has been attributed to the reconstruction of surface defects[32]. The stable CO oxidation at Pt-SnO_2/C was supported by chronoamperometry with a steady current for 0.5 h at 0.4 V (**Figure S32**). Transferring the rotation-rate-dependent and stable CO continuous oxidation on Pt-SnO_2 to the proposed mechanism in eq. 1 reveals that the (SnO_2)Sn-OH and (SnO_2)Sn* are interconvertible with relatively fast kinetics during CO oxidation in a potential window of 0.3 – 0.6 V.

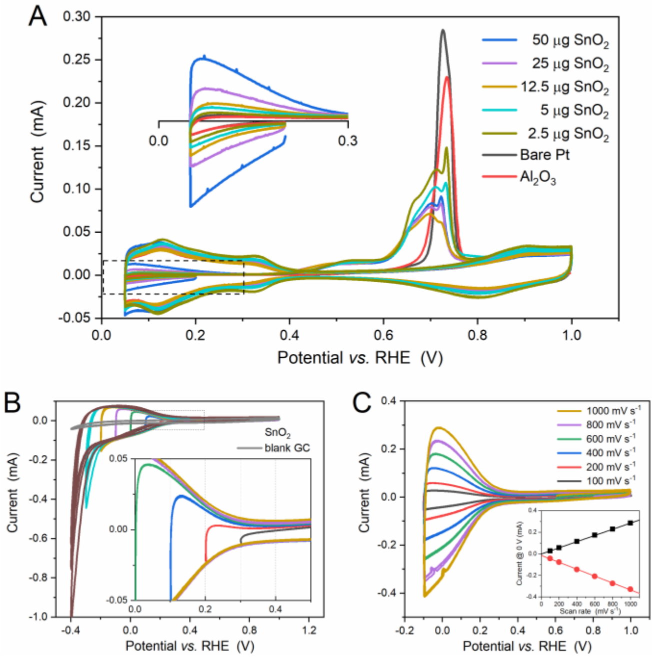

Figure 8. (A) CO stripping voltammograms of SnO_2 nanopowder on a polycrystalline Pt disc electrode (5 mm diameter) with a scan rate of 50 mV s^{-1} and with the SnO_2 loading varied by adding different amounts of SnO_2. The inset magnifies the $H_{ads/des}$ region on the first cycles of the voltammograms. The voltammogram of Al_2O_3 on Pt is also present for comparison. (B) The window-opening and (C) scan-rate-dependent cyclic voltammograms of SnO_2 nanopowder on a glassy carbon electrode (GC, 5 mm diameter), with the inset showing the linear relationship between the current at 0 V and the corresponding scan rate. In the window-opening experiment, the scan rate is 200 mV s^{-1} and the blank (GC) data is also present as a reference.

Now the question turns to the electrochemistry of the SnO_2 surface. As suggested by the proposed bifunctional mechanism of Pt-SnO_2, a redox reaction of (SnO_2)Sn-OH and (SnO_2)Sn* is expected at potentials around the onset of CO oxidation (~0.3 V), but neither Pt-SnO_2/C nor the physical mixtures between SnO_2 and Pt/C shows any evidence relating to SnO_2 in the voltammograms. The double-layer charging from the carbon support may obscure the voltammetric features. Thus, commercial SnO_2 nanopowders were directly loaded on Pt and glassy carbon (GC) electrodes.

Figure 8A shows CO stripping voltammograms of SnO_2 deposited on a Pt disc electrode with different loadings of SnO_2 nanopowders. On the whole, similar effects of SnO_2, as observed for Pt-SnO_2/C and the Pt/C-SnO_2 physical mixtures, are found on these SnO_2-modified Pt electrodes (unaffected $H_{ads/des}$ features in shape, low onset potentials for CO_{ads} oxidation, and a SnO_2-coverage-induced charge distribution between the main peak and the pre-peak). Closer examination of the $H_{ads/des}$ features region of the first sweep, in which Pt electrochemistry is completely blocked by CO_{ads}, reveals an unconventional pseudo-capacitance, the charge of which increases proportionally to the SnO_2 loading.

The electrochemistry of SnO_2 was then studied on a SnO_2-modified glassy carbon (GC) electrode. **Figure 8B** and **8C** show window-opening and scan-rate dependent voltammograms, respectively. The pseudo-capacitance of SnO_2 is repeatable on

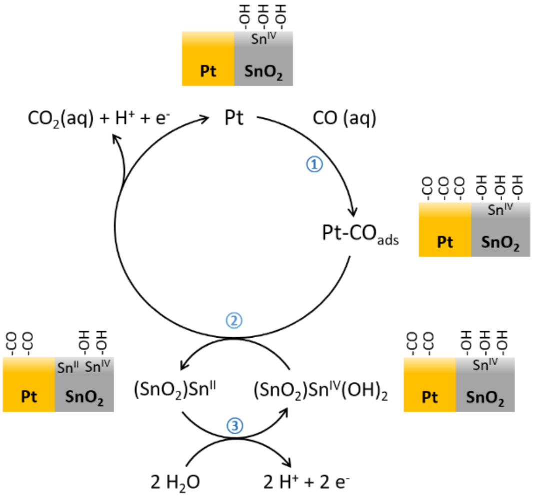

Figure 9. Catalysis cycle of CO oxidation on Pt with the co-catalyst SnO_2.

GC in the same potential region and found to be related to a highly reversible and surface-bounded redox couple. The redox couple is operative between -0.2 – 0.3 V, and its kinetics allows a symmetric peak shape to be maintained at sweep rates up to 1 V s^{-1}. According to the well-accepted dual valency of Sn in tin oxide chemistry[23, 27a] and the standard electrode potential data of Sn[17], the redox couple is attributed to the reversible interconversion between Sn^{IV} and Sn^{II} on the SnO_2 surface. Further decreasing the potential drives the irreversible transformation from Sn^{IV} to Sn^{II}, or even Sn^{II} to Sn^0. The presence of the reversible Sn^{IV}/Sn^{II} redox couple is in agreement with the surface reduction of SnO_2 in H_2(g) as suggested by XAS, and more importantly corroborates the proposed bifunctional mechanism from SnO_2. Thus, the regeneration of Sn-OH, following the L-H reaction of CO oxidation (eq.1), can tentatively be written as

$$(SnO_2)Sn^{IV}(OH)_2 + 2\,H^+ + 2e^- \rightleftharpoons (SnO_2)Sn^{II} + 2\,H_2O \qquad \text{(eq.2)}$$

It should be noted that the exact coordination structure of this Sn^{IV}/Sn^{II} couple is unclear and that the double coordinated OH in $Sn^{IV}(OH)_2$ is only used to balance the change of the Sn oxidation state in eq. 2.

From the voltammetry studies presented above, SnO_2 is suggested to enable CO oxidation at a low overpotential by providing Sn-OH. Assuming the SnO_2 component of the Pt-SnO_2 interface has a similar nature to that of plain SnO_2, the bifunctional mechanism at Pt-SnO_2 can be attributed to the co-catalysis of SnO_2, in which the Sn-OH is constantly supplied by a reversible redox couple located on the surface of SnO_2. By such a mechanism, the catalysis cycle of CO oxidation, disconnected on the pure Pt surface due to unfavourable formation of Pt-OH_{ads} at low potential[2d, 4a], is completed on Pt-SnO_2 (**Figure 9**). Dissolved CO molecules chemisorb on active Pt sites, forming Pt-CO_{ads} (step ①), and then the CO_{ads} reacts with Sn-OH species (step ②), releasing CO_2, a free Pt site and a Sn^{II} that can be oxidised back to Sn-OH species at the same potential (step ③).

As both the SnO_2-promoted CO oxidation and the redox reaction of Sn^{IV}/Sn^{II} involve the formation/cleavage of Sn^{IV}-OH, the appropriate Sn^{IV}-OH energetics, or matching between these reactions in potential, may be responsible for the unique property of SnO_2 for CO oxidation at low overpotentials. To support this hypothesis, two other metal oxide nanoparticles, Al_2O_3 (**Figure 8A**) and TiO_2 (P25, **Figure S33**) deposited on Pt disc electrodes were measured. The deposition of these two metal oxides shows site-blocking effects on Pt rather than any promotional effects. On TiO_2-modified GC electrodes a reversible redox couple relating to Ti^{IV}/Ti^{III} [33] is found at a potential close to but more negative (< -0.1 V) than that of SnO_2 (**Figure S34**), suggesting that a stronger driving force is required to dissociate the Ti^{IV}-OH bond. Similarly, the effects of other oxides have previously been investigated. CeO_2, which has a redox couple of Ce^{IV}/Ce^{III} > 1 V[34], was reported to show no promotional effect when being loaded on Pt[35]. Recently, Olu *et al*. studied enhanced CO oxidation activity on Pt electrodes modified by RuO_2 nanosheets [36] and by WO_3 nanoparticles[37], but different promotional mechanisms were found. The RuO_2 forms 'Ru metal-like' sites that provide ligand effects to Pt and additional sites for CO absorption[36], and the WO_3, the hydroxyl formation on which is less reversible than that of SnO_2, can only assist in the removal of weakly adsorbed CO_{ads} via a bifunctional-type reaction [37].

Conclusion

A Pt-SnO_2/C catalyst was designed to study the role of SnO_2 in the bifunctional mechanism of CO oxidation. Using the analytical capabilities of electron microscopy and the equipped spectroscopies, the distribution of the Pt and SnO_2 nanoparticles were observed and found to be present as two forms, isolated Pt nanoparticles on carbon and Pt-SnO_2 nanoparticles clusters, comprising ~2 nm Pt and SnO_2 nanoparticles in contact with each other. The Sn speciation of Pt-SnO_2/C was interrogated by XRD and detailed XAS analysis. XRD and XAS (measured in air) suggest that in the as-prepared samples SnO_2 is the dominate Sn species (>99 at% out of total Sn), and when measured in H_2(g) the XAS suggests that the SnO_2 was reduced, corresponding to surface-reduced SnO_2 species rather than alloyed Sn or SnO.

CO stripping voltammetry on the Pt-SnO_2/C shows that the CO oxidation is strongly promoted, with an onset potential of ~0.3 V and significant contribution in the pre-peak region. Such promotional effects of SnO_2 were corroborated by comparison to Pt-SnO_2 surfaces constructed from mixtures of Pt/C and SnO_2 nanoparticles and SnO_2-modified Pt electrodes. CO continuous oxidation voltammetry of Pt-SnO_2/C suggests that CO oxidation on Pt-SnO_2 at low overpotentials is so fast that the diffusion of dissolved CO becomes the rate-determining-step beyond ~0.4 V, and that a redox couple continuously supplying the necessary Sn-OH species exists at Pt-SnO_2 to maintain the diffusion-determined current. The presence of a reversible Sn^{IV}/Sn^{II} redox couple between -0.2–0.3 V was found in voltammetric studies on SnO_2-modified GC electrodes. We, therefore, propose that the bifunctional mechanism of Pt-SnO_2 originates from the co-catalysis role of SnO_2, in which Sn-OH species are consumed in reacting Pt-CO_{ads} at the interface and regenerated by dissociating water. The unique promotional effect of SnO_2 were then discussed in relation to the appropriate energetics of the metal-hydroxide bond. As the promotional effect does not rely on the modification of the Pt electronic structure, the CO-tolerant Pt-SnO_2 is expected to have unique catalytical properties for alcohol oxidation.

Experimental Section

Hexachloroplantic acid ($H_2PtCl_6 \cdot 6H_2O$, 99.999% metals basis) and tin(IV) oxide nanopowder (SnO_2, >99.9%, 8-10 nm) were purchased from Alfa Aesar. Representative results from X-ray diffraction (XRD) and transmission electron microscopy (TEM) imaging analysis of the SnO_2 nanopowder are shown in **Figure S1**. Sodium stannate trihydrate ($Na_2SnO_3 \cdot 3H_2O$, 95%), sodium hydroxide (NaOH, ≥98%) and Nafion perfluorinated resin solution (5 wt%) were purchased from Sigma Aldrich. Vulcan XC-72R carbon and commercial Pt/C (20 wt%) were supplied by Cabot and Johnson Matthey, respectively. High-purity N_2 (≥99.998%), H_2 (≥99.999%), and CO (≥99.9%) were supplied by BOC. All materials were used as received.

100 mg Vulcan XC-72R carbon was dispersed into 200 mL ultrapure water (18.2 MΩ) by sonication for 1 h. To the colloid solution, a H_2PtCl_6 solution (~0.2 M), NaOH solution (~0.2 M) at 4 molar equivalent to H_2PtCl_6, and Na_2SnO_3 solution were introduced stepwise with an interval of 5 min sonication and 30 min stirring. The resultant solution was heated under reflux at 90 °C for 1 h, then allowed to settle overnight. The solid product was collected via centrifugation and washed three times with water before being dried under vacuum. The total metal loading (Pt + Sn) on the carbon was controlled to be 20 wt%. Using the same method, PtO_x-SnO_2/C catalysts with nominal Pt/Sn molar ratios of 3/1 and 1/3, as well as PtO_x/C, were synthesised.

PtO_x/C and PtO_x-SnO_2/C were reduced into Pt/C and Pt-SnO_2/C, respectively, by exposure to H_2 (g) at room temperature. The reduction was carried out in an air-tight cell fitted to a flow regulator and gas bubbler (**Figure S2**). N_2, H_2, and N_2 gases (40 mL min^{-1}) were purged through each sample consecutively for 20 min periods. The resultant samples were stored in air-tight vials. **Caution – the reduced sample in H_2 should not be directly exposed to air – fire risk.**

Scanning electron microscopy (SEM) together with energy-dispersive X-ray (EDX) analysis (SEM-EDX, FEI XL30 ESEM equipped with an Ultradry detector and JEOL JSM5400 SEM equipped with an Oxford INCA x-sight 7418 EDS probe) and thermogravimetric analysis (Netzch TG209) under 40 mL min^{-1} O_2/Ar were carried out to determine the composition and metal loading of the as-prepared samples. For our targeted sample Pt-SnO_2/C, the atomic ratio of Pt to Sn, and the loadings of Pt and SnO_2 are 2.62 ± 0.12, ~12.3 wt% and ~4.0 wt%, respectively. The morphology and the size of the deposited metal nanoparticles were imaged using a transmission electron microscope (TEM; FEI, Tecnai T12) at 80 kV. X-ray diffraction (XRD) patterns were obtained using a Bruker D2 Phaser diffractometer with Cu K_α radiation (λ = 1.5418 Å) and a LYNXEYE detector.

Scanning transmission electron microscopy (STEM) measurements were carried out on an aberration-corrected Nion UltraSTEM 100MC at the SuperSTEM Laboratory (Daresbury, UK). The microscope was operated with an accelerating voltage of 60 kV, using a 31.5 mrad beam convergence semi-angle for an electron probe size of about 1 Å. The electron energy loss (EEL) spectrometer collection semi-angle was 44 mrad and, the bright field (BF) and high-angle annular dark field (HAADF) detector angular ranges were 0-14 mrad and 100-230 mrad, respectively. Sn $M_{4,5}$ (onset 485 eV) and O K (onset 532 eV) ionization edge spectrum images were acquired with an energy dispersion of 0.6 eV per channel and an acquisition time of 0.02 s per spectrum. Due to its high energy onset at 2202 eV, it was more practical to acquire Pt $M_{4,5}$ edge spectrum images separately from those covering the Sn $M_{4,5}$ and O K edges, maintaining the same dispersion (0.6 eV per channel), but increasing the exposure time to 0.5 s. EELS spectrum images were de-noised using Principal Component Analysis (PCA) as implemented in the MSA plugin for Gatan's Digital Micrograph Suite. The MSA plugin is commercially available from HREM research. EELS signal maps were obtained by integrating the intensity over a window of 485–530 eV for Sn $M_{4,5}$ and of 2150–2300 eV for Pt $M_{4,5}$, after background subtraction using a conventional power-law model over a window of 420–480 eV for Sn $M_{4,5}$ and of 2000–2100 eV for Pt $M_{4,5}$. Red (Pt $M_{4,5}$) and green (Sn $M_{4,5}$ and O K) colour maps in **Figure 1F, Figure S7C, Figure S8B** and **Figure S9C** are superimposed from the complementary datasets from the same sample regions.

X-ray absorption spectra were acquired at the B18 beamline of the Diamond Light Source (UK) using a Quick EXAFS mode with a ring energy of 3.0 GeV and a ring current of 299–302 mA. Each sample was finely ground and mixed with boron nitride to form a homogeneous mixture, and then compressed into a pellet. The pellets were measured in transmission mode by ionization chambers at the Pt L_3 and Sn K edges, along with a corresponding foil in the reference channel. The measurements were conducted in an airtight gas cell under H_2(g), unless otherwise indicated and for the oxide reference samples, which were measured in air. The measured spectra were processed and analysed using ATHENA and ARTEMIS (both in the Demeter software package)[38], respectively. The energy shift of each spectrum was calibrated in two steps: choosing the first peak in the derivative of both the sample spectrum and the corresponding reference spectrum as E_0, and then assigning the E_0 of the reference spectrum to the tabulated value provided by ATHENA. The edge step of each sample was normalized by subtracting the linear pre-edge and quadratic post-edge function, and the ranges of pre-edge and post-edge are chosen as the same for each edge. The background in the extended X-ray absorption fine structure (EXAFS) region was subtracted using the AUTOBKG algorithm. The multiple-shell EXAFS fitting was carried out on Pt L_3 edge data using a model based on the face-cubic structure of Pt. The same model was applied to a Pt foil spectrum to obtain the amplitude reduction factor of Pt, 0.84. Similarly, the amplitude reduction factor of Sn is 1.03, obtained by a two-shell fit of a SnO_2 reference sample. The Fourier transformation from EXAFS spectra in k space to those in R space was conducted over a k range of 3.0–15.0 Å^{-1} for the Pt L_3 edge and a k range of 3.5–13.4 Å^{-1} for the Sn K edge. The spectra in R space, presented in the text, are not phase-corrected.

Electrochemical measurements were performed on a standard three-electrode cell connected to a PGSTAT12 potentiostat (Metrohm Autolab, with a SCANGEN module). A Pt gauze was used as the counter electrode, and a home-made reversible hydrogen electrode (RHE) equipped with a Luggin capillary as the reference electrode. The RHE consists of a Pt gauze electrode over which a slow yet continuous stream of H_2 (g) bubbles were passed, using the same electrolyte as the main cell compartment. The values of potentials in the text are referenced against this RHE, unless stated otherwise.

For powder catalysts, the working electrode was prepared by drop-casting 10 µL of a catalyst ink onto an inverted polished glassy carbon (GC) electrode (5 mm diameter, Pine) and drying at 700 rpm and under an IR lamp (250 W). The catalyst ink was prepared by dispersing 2 mg of each sample into 1 mL isopropanol alcohol (IPA) aqueous solution (20 vol% of IPA). The catalyst inks of Pt/C-SnO_2 physical mixtures were prepared by dispersing SnO_2 into a commercial Pt/C ink whilst maintaining the concentration of Pt/C as 2 mg mL^{-1}. Prior to measurements, the prepared working electrodes were conditioned in N_2-purged 0.1 M $HClO_4$ (Suprapur, Merck) by cycling between 50 mV and 800 mV for at least 10 cycles with a scan rate of 100 mV s^{-1}.

For the CO stripping voltammetry, CO was bubbled into degassed 0.1 M $HClO_4$ for 20 min whilst the potential of the prepared working electrode was held at 0.2 V. Subsequently, N_2 was purged for another 20 min to remove CO from the electrolyte and the potential was then swept to 0.05 V at a scan rate of 20 mV s^{-1} and then cycled between 0.05 V and 1 V for 3 cycles with the same scan rate.

Oxide modified Pt and GC electrodes were also used as working electrodes. Each metal oxide, SnO_2 (8–10 nm, Alfa Aesar), Al_2O_3 (0.05 µm, BUEHLER) or TiO_2 (P25), was loaded onto a Pt electrode (5 mm diameter, Pine) or a polished glassy carbon (GC) electrode (5mm diameter) using the drop-casting method as described above. Metal oxide suspensions were prepared by sonicating 5 mg of each metal oxide in 1 mL IPA aqueous solution (40 vol% of IPA). Each bare Pt electrode was polished and then conditioned by cycling between 0.05–1.40 V in N_2-purged 0.1 M $HClO_4$ with 200 mV s^{-1} for at least 40 cycles. Before electrochemical measurements, the modified Pt and GC electrodes were conditioned over a narrower potential window (0.05–1.0 V). The CO stripping voltammetry on the Pt electrodes was carried out at a scan rate of 50 mV s^{-1}.

Acknowledgements

HH acknowledges Fellowship support from the China Scholarship Council (201608440295) and the University of Southampton. XAS data were collected at Diamond on B18 as part of the UK Catalysis Hub BAG allocation (SP15151-9 and SP15151-10). SuperSTEM is the UK National Research Facility for Advanced Electron Microscopy, supported by the Engineering and Physical Sciences Research Council (EPSRC).

Keywords: Bifunctional mechanism • Pt-SnO$_2$ • SnO$_2$ • CO oxidation • electrocatalysts

[1] a) H. A. Gasteiger, N. M. Markovic, P. N. Ross, *J. Phys. Chem.* **1995**, *99*, 8945-8949; b) H. A. Gasteiger, N. M. Marković, P. N. Ross, *Catal. Lett.* **1996**, *36*, 1-8.

[2] a) Q. Wang, G. Q. Sun, L. H. Jiang, Q. Xin, S. G. Sun, Y. X. Jiang, S. P. Chen, Z. Jusys, R. J. Behm, *Phys. Chem. Chem. Phys.* **2007**, *9*, 2686-2696; b) S. X. Liu, L. W. Liao, Q. Tao, Y. X. Chen, S. Ye, *Phys. Chem. Chem. Phys.* **2011**, *13*, 9725-9735; c) M. Heinen, Z. Jusys, R. J. Behm, in *Handbook of Fuel Cells*, **2010**; d) M. T. M. Koper, S. C. S. Lai, E. Herrero, in *Fuel Cell Catalysis*, **2009**, pp. 159-207.

[3] G. Garcia, M. T. Koper, *ChemPhysChem* **2011**, *12*, 2064-2072.

[4] a) N. Markovic, *Surf. Sci. Rep.* **2002**, *45*, 117-229; b) E. Antolini, E. R. Gonzalez, *Electrochim. Acta* **2010**, *56*, 1-14; c) Y. Liu, D. Li, V. R. Stamenkovic, S. Soled, J. D. Henao, S. Sun, *ACS Catal.* **2011**, *1*, 1719-1723; d) Z. Liu, G. S. Jackson, B. W. Eichhorn, *Angew. Chem., Int. Ed.* **2010**, *49*, 3173-3176.

[5] a) B. E. Hayden, M. E. Rendall, O. South, *J. Am. Chem. Soc.* **2003**, *125*, 7738-7742; b) M. Watanabe, M. Shibata, S. Motoo, *J. Electroanal. Chem. Interfacial Electrochem.* **1985**, *187*, 161-174.

[6] a) V. R. Stamenkovic, M. Arenz, C. A. Lucas, M. E. Gallagher, P. N. Ross, N. M. Markovic, *J. Am. Chem. Soc.* **2003**, *125*, 2736-2745; b) V. Stamenkovic, M. Arenz, B. B. Blizanac, K. J. J. Mayrhofer, P. N. Ross, N. M. Markovic, *Surf. Sci.* **2005**, *576*, 145-157.

[7] a) B. E. Hayden, M. E. Rendall, O. South, *J. Mol. Catal. A: Chem.* **2005**, *228*, 55-65; b) A. N. Haner, P. N. Ross, *J. Phys. Chem.* **1991**, *95*, 3740-3746; c) G. Stalnionis, L. Tamašauskaitė-Tamašiūnaitė, V. Pautienienė, A. Sudavičius, Z. Jusys, *J. Solid State Electrochem.* **2004**, *8*, 892-899.

[8] a) E. Antolini, E. R. Gonzalez, *Catal. Today* **2011**, *160*, 28-38; b) X. Lu, Z. Deng, C. Guo, W. Wang, S. Wei, S. P. Ng, X. Chen, N. Ding, W. Guo, C. M. Wu, *ACS Appl. Mater. Interfaces* **2016**, *8*, 12194-12204.

[9] a) J. M. Jin, T. Sheng, X. Lin, R. Kavanagh, P. Hamer, P. Hu, C. Hardacre, A. Martinez-Bonastre, J. Sharman, D. Thompsett, W. F. Lin, *Phys. Chem. Chem. Phys.* **2014**, *16*, 9432-9440; b) L. Calvillo, L. Mendez De Leo, S. J. Thompson, S. W. T. Price, E. J. Calvo, A. E. Russell, *J. Electroanal. Chem.* **2018**, *819*, 136-144.

[10] a) Y. Lin, S. Zhang, S. Yan, G. Liu, *Electrochim. Acta* **2012**, *66*, 1-6; b) M. Arenz, V. Stamenkovic, B. Blizanac, K. Mayrhofer, N. Markovic, P. Ross, *J. Catal.* **2005**, *232*, 402-410; c) F. Ye, J. Li, T. Wang, Y. Liu, H. Wei, J. Li, X. Wang, *J. Phys. Chem. C* **2008**, *112*, 12894-12898.

[11] H. Huang, A. Nassr, V. Celorrio, S. F. R. Taylor, V. K. Puthiyapura, C. Hardacre, D. J. L. Brett, A. E. Russell, *Faraday Discuss.* **2018**, *208*, 555-573.

[12] a) G. Wang, T. Takeguchi, T. Yamanaka, E. N. Muhamad, M. Mastuda, W. Ueda, *Appl. Catal., B* **2010**, *98*, 86-93; b) D. R. M. Godoi, J. Perez, H. M. Villullas, *J. Power Sources* **2010**, *195*, 3394-3401.

[13] E. M. Crabb, R. Marshall, D. Thompsett, *J. Electrochem. Soc.* **2000**, *147*, 4440-4447.

[14] S. Speller, U. Bardi, in *The Chemical Physics of Solid Surfaces, Vol. 10* (Ed.: D. P. Woodruff), Elsevier, **2002**, pp. 184-224.

[15] a) W. D. Michalak, J. M. Krier, S. Alayoglu, J.-Y. Shin, K. An, K. Komvopoulos, Z. Liu, G. A. Somorjai, *J. Catal.* **2014**, *312*, 17-25; b) J. L. Margitfalvi, I. Borbáth, M. Hegedűs, E. Tfirst, S. Gőbölös, K. Lázár, *J. Catal.* **2000**, *196*, 200-204; c) M. Vandichel, A. Moscu, H. Grönbeck, *ACS Catal.* **2017**, *7*, 7431-7441.

[16] K. J. Cathro, *J. Electrochem. Soc.* **1969**, *116*, 1608-1611.

[17] P. Vanysek, in *CRC handbook of chemistry and physics, Vol. 87*, **1998**.

[18] A. Rabis, D. Kramer, E. Fabbri, M. Worsdale, R. Kötz, T. J. Schmidt, *J. Phys. Chem. C* **2014**, *118*, 11292-11302.

[19] a) D.-H. Lim, D.-H. Choi, W.-D. Lee, H.-I. Lee, *Appl. Catal., B* **2009**, *89*, 484-493; b) D.-H. Lim, D.-H. Choi, W.-D. Lee, D.-R. Park, H.-I. Lee, *Electrochem. Solid-State Lett.* **2007**, *10*, B87-B90.

[20] T. Matsui, K. Fujiwara, T. Okanishi, R. Kikuchi, T. Takeguchi, K. Eguchi, *J. Power Sources* **2006**, *155*, 152-156.

[21] a) M. S. Holt, W. L. Wilson, J. H. Nelson, *Chem. Rev.* **1989**, *89*, 11-49; b) O. I. Milner, G. F. Shipman, *Anal. Chem.* **1955**, *27*, 1476-1478.

[22] a) D. Y. DeSario, F. J. DiSalvo, *Chem. Mater.* **2014**, *26*, 2750-2757; b) W. Du, G. Yang, E. Wong, N. A. Deskins, A. I. Frenkel, D. Su, X. Teng, *J. Am. Chem. Soc.* **2014**, *136*, 10862-10865; c) F. Humblot, F. Lepeltier, J. P. Candy, J. Corker, O. Clause, F. Bayard, J. M. Basset, *J. Am. Chem. Soc.* **1998**, *120*, 137-146.

[23] M. Batzill, U. Diebold, *Prog. Surf. Sci.* **2005**, *79*, 47-154.

[24] a) A. López-Cudero, J. Solla-Gullón, E. Herrero, A. Aldaz, J. M. Feliu, J. Electroanal. Chem. 2010, 644, 117-126; b) S. Guerin, B. E. Hayden, C. E. Lee, C. Mormiche, J. R. Owen, A. E. Russell, B. Theobald, D. Thompsett, J Comb Chem 2004, 6, 149-158.

[25] a) M. J. S. Farias, W. Cheuquepán, A. A. Tanaka, J. M. Feliu, *ACS Catal.* **2017**, *7*, 3434-3445; b) R. Rizo, E. Pastor, M. T. M. Koper, *J. Electroanal. Chem.* **2017**, *800*, 32-38.

[26] T. Takeguchi, A. Kunifuji, N. Narischat, M. Ito, H. Noguchi, K. Uosaki, S. R. Mukai, *Catal. Sci. Technol.* **2016**, *6*, 3214-3219.

[27] a) S. Das, V. Jayaraman, *Prog. Mater. Sci.* **2014**, *66*, 112-255; b) H. Tamura, K. Mita, A. Tanaka, M. Ito, *J. Colloid Interface Sci.* **2001**, *243*, 202-207.

[28] a) D. R. Schryer, B. T. Upchurch, B. D. Sidney, K. G. Brown, G. B. Hoflund, R. K. Herz, *J. Catal.* **1991**, *130*, 314-317; b) D. R. Schryer, B. T. Upchurch, J. D. Van Norman, K. G. Brown, J. Schryer, *J. Catal.* **1990**, *122*, 193-197.

[29] S. Gilman, *J. Phys. Chem.* **1964**, *68*, 70-80.

[30] J. S. Spendelow, J. D. Goodpaster, P. J. Kenis, A. Wieckowski, *J. Phys. Chem. B* **2006**, *110*, 9545-9555.

[31] C. A. Angelucci, E. Herrero, J. M. Feliu, *J. Phys. Chem. C* **2010**, *114*, 14154-14163.

[32] a) D. S. Strmcnik, D. V. Tripkovic, D. van der Vliet, K. C. Chang, V. Komanicky, H. You, G. Karapetrov, J. P. Greeley, V. R. Stamenkovic, N. M. Markovic, *J. Am. Chem. Soc.* **2008**, *130*, 15332-15339; b) J. Inukai, D. A. Tryk, T. Abe, M. Wakisaka, H. Uchida, M. Watanabe, *J. Am. Chem. Soc.* **2013**, *135*, 1476-1490; c) A. V. Rudnev, A. Kuzume, Y. Fu, T. Wandlowski, *Electrochim. Acta* **2014**, *133*, 132-145.

[33] a) L. A. Lyon, J. T. Hupp, *J. Phys. Chem. B* **1999**, *103*, 4623-4628; b) K. R. Reyes-Gil, Z. D. Stephens, V. Stavila, D. B. Robinson, *ACS Appl. Mater. Interfaces* **2015**, *7*, 2202-2213.

[34] a) S. A. Hayes, P. Yu, T. J. O'Keefe, M. J. O'Keefe, J. O. Stoffer, *J. Electrochem. Soc.* **2002**, *149*, C623-C630; b) N. Padmanathan, S. Selladurai, *Ionics* **2014**, *20*, 409-420.

[35] Y. Katayama, T. Okanishi, H. Muroyama, T. Matsui, K. Eguchi, *ACS Catal.* **2016**, *6*, 2026-2034.

[36] P.-Y. Olu, T. Ohnishi, D. Mochizuki, W. Sugimoto, *J. Electroanal. Chem.* **2018**, *810*, 109-118.

[37] P.-Y. Olu, T. Ohnishi, Y. Ayato, D. Mochizuki, W. Sugimoto, *Electrochem. Commun.* **2016**, *71*, 69-72.

[38] B. Ravel, M. Newville, *J. Synchrotron Radiat.* **2005**, *12*, 537-541.

Entry for the Table of Contents

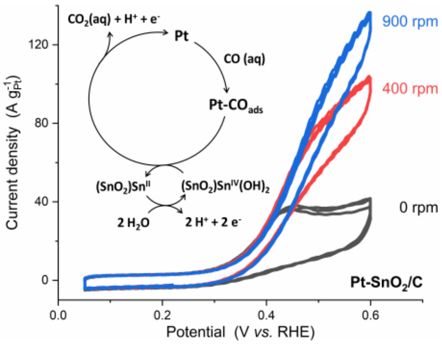

The CO oxidation is strongly promoted on Pt-SnO_2 interfaces (Pt-SnO_2/C, mixtures of Pt/C and SnO_2 nanoparticles, and SnO_2-modified Pt electrodes). The kinetics at low overpotential is so fast that the diffusion of dissolved CO becomes the rate-determining-step beyond ~0.45 V_{RHE}. By identifying a redox couple of Sn^{IV}/Sn^{II} on the SnO_2 surface, the promotional mechanism of Pt-SnO_2 is attributed to the co-catalysis role of SnO_2.

Supporting information

The role of SnO_2 in the bifunctional mechanism of CO oxidation at Pt-SnO_2 electrocatalysts

Haoliang Huang[a], Edward T.C. Hayes[a], Diego Gianolio[b], Giannantonio Cibin[b], Fredrik S. Hage[c], [d], Quentin M. Ramasse[c], [e] and Andrea E. Russell*[a]

---

[a] Dr. H. Huang, Mr. E.T.C. Hayes, Prof. A.E. Russell
School of Chemistry, University of Southampton, Highfield, Southampton SO17 1BJ, United Kingdom
E-mail: a.e.russell@soton.ac.uk
[b] Dr. D. Gianolio and Dr. G. Cibin
Diamond Light Source Ltd, Diamond House, Harwell Campus, Didcot OX11 0DE, United Kingdom
[c] Dr. F.S. Hage and Prof. Q.M. Ramasse
SuperSTEM Laboratory, SciTech Daresbury Campus, Daresbury WA4 4AD, United Kingdom
[d] Dr. F.S. Hage
Department of Physics / Centre for Materials Science and Nanotechnology, University of Oslo, NO-0318 Oslo, Norway
[e] Prof. Q.M. Ramasse
School of Physics and Astronomy and School of Chemical and Process Engineering, University of Leeds, Leeds LS2 9JT, United Kingdom

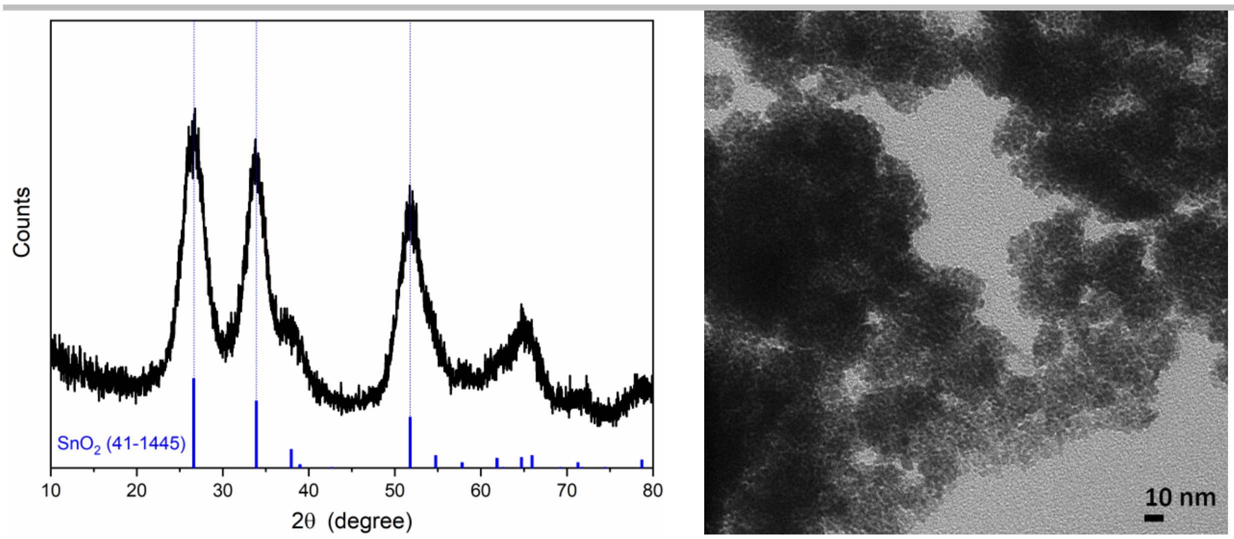

Figure S1 (left) XRD pattern and (right) a typical TEM image of SnO_2 nanopowder (8–10 nm, Alfa Aesar), showing that the actual particles size is largely consistent with the provided specifications and that the SnO_2 nanoparticles tend to aggregate. The standard pattern of rutile SnO_2 (41-1445) was obtained from the JCPDS database.

Figure S2 A schematic illustration of the setup for H_2(g) reduction at room temperature. The sample powder was placed in an air-tight vial (left) fitted to a flowmeter and a gas bubbler (right). N_2, H_2 and N_2 gases were purged consecutively for 20 min periods.

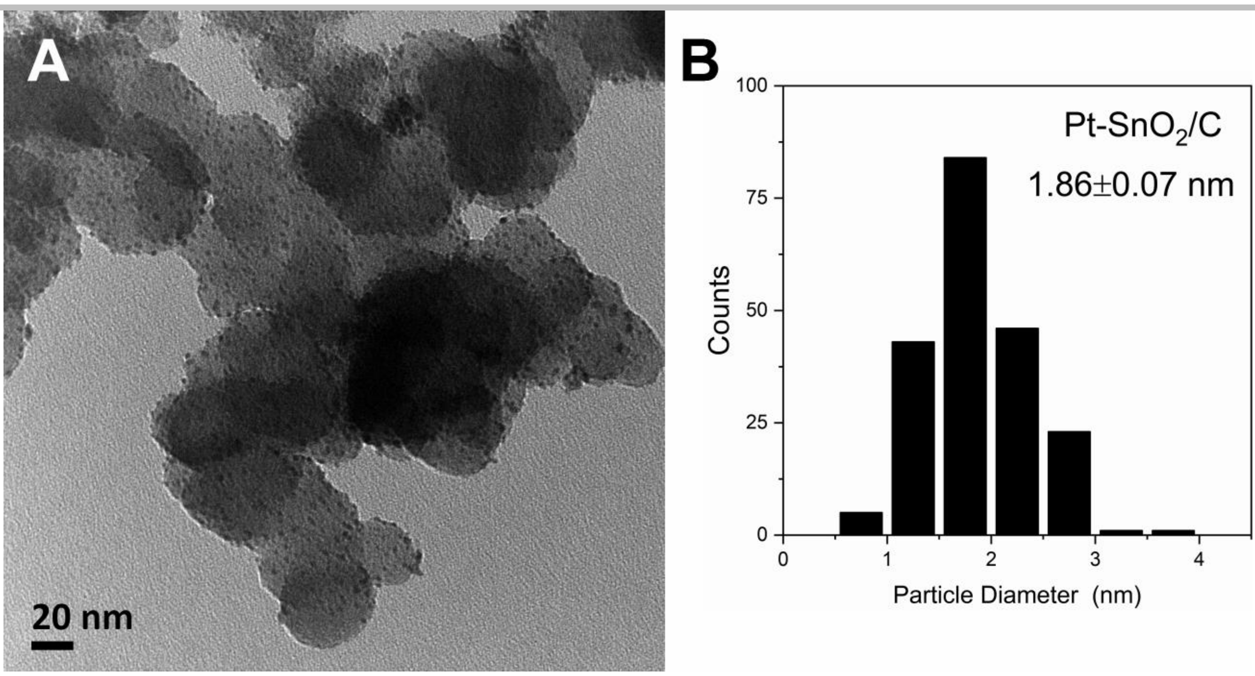

Figure S3 A representative TEM image of Pt-SnO_2/C at a low magnification, along with a histogram of particle size distribution.

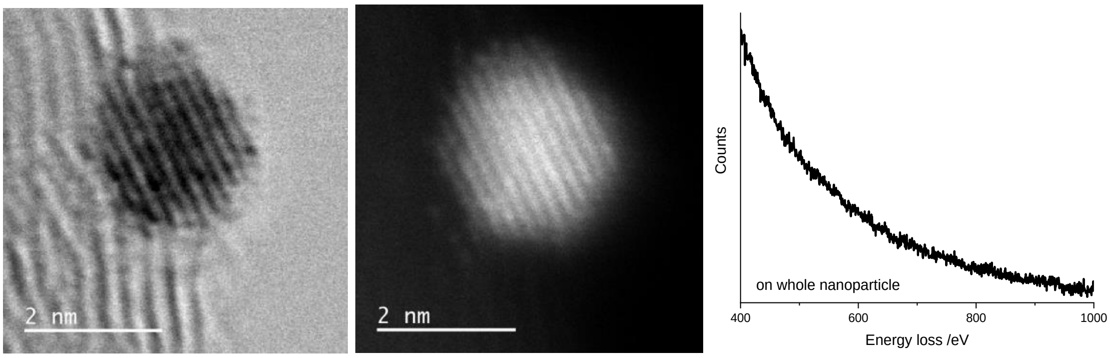

Figure S4. (left) representative STEM-BF and (middle) STEM-HAADF images of an isolated particle of Pt from Pt-SnO_2/C, and (right) an EELS spectrum (without background subtraction) integrated over the whole particle, showing that no signal for Sn and O edges can be detected.

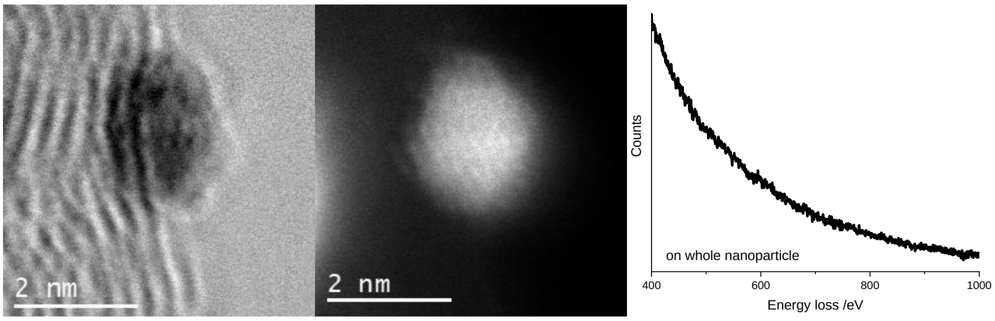

Figure S5. Same as **Figure S4** but from a different region.

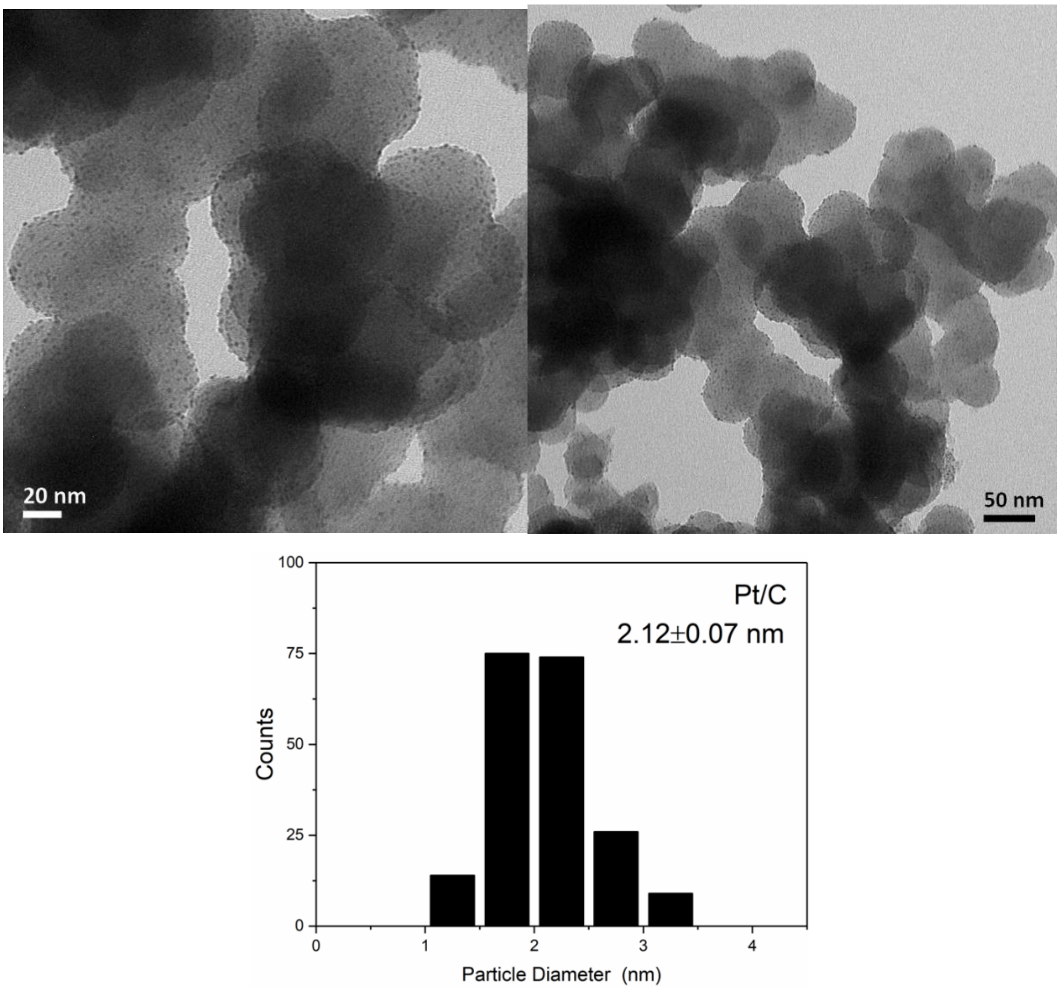

Figure S6. (top) TEM images of the as-prepared Pt/C at two magnifications, and (bottom) the corresponding particle size distribution with at least 200 nanoparticles measured. The Pt/C was synthesised using the same method as the Pt-SnO_2/C.

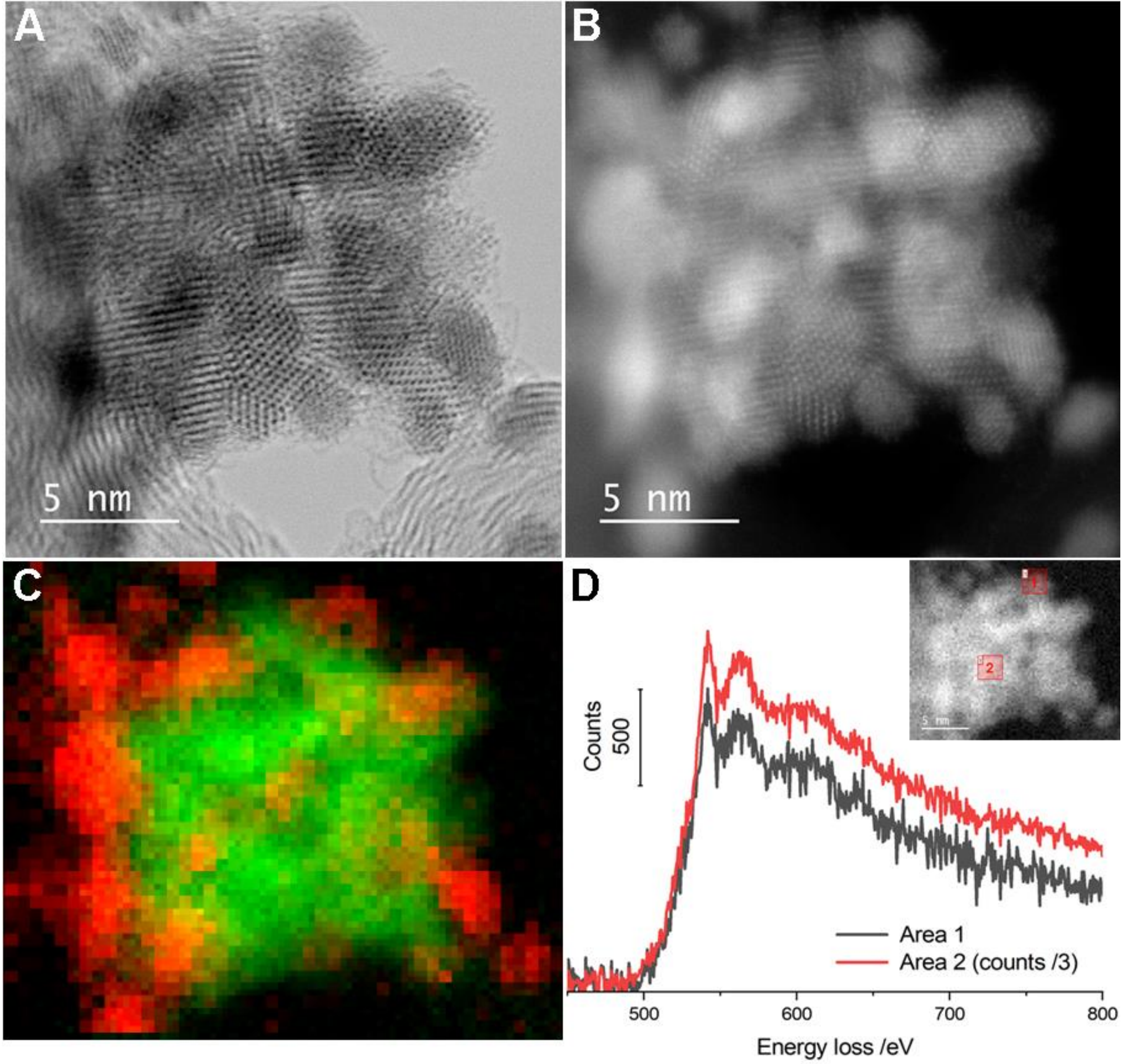

Figure S7. (A) STEM-BF and (B) STEM-HAADF images of a nanoparticle cluster region of Pt-SnO_2/C. (C) EELS mapping image of Pt *M*$_{4,5}$ edge (red), and of Sn $M_{4,5}$ edge and O *K* edge (green – both elements are mapped together). (D) EELS spectra extracted from the areas marked in the inset. The data here are consistent with **Figure 1F**.

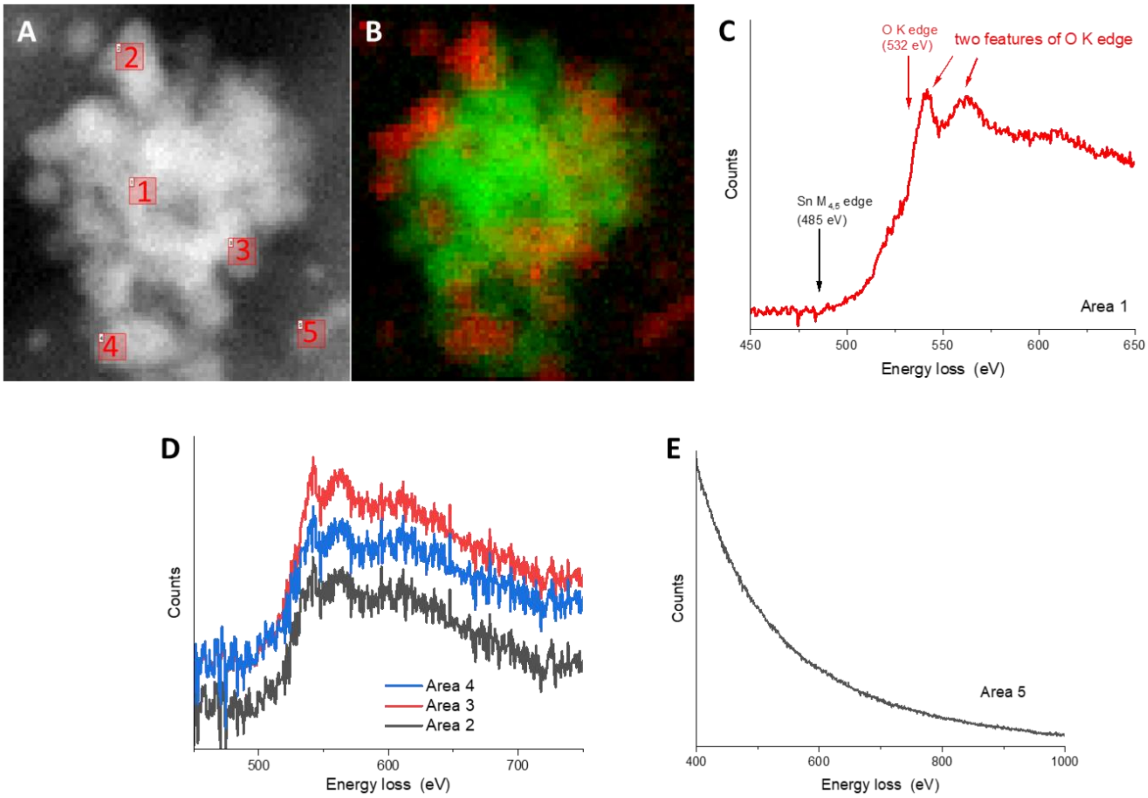

Figure S8. (A) The STEM-HAADF image and (B) EELS elemental mapping as shown in **Figure 1F**: Pt $M_{4,5}$ edge (red), and overlapped edges of Sn $M_{4,5}$ and O K (green). (C–E) EELS spectra extracted from the regions labelled in the HAADF image of the selected areas, ranging from tin oxide-rich region to the Pt-rich region. The spectrum from area 5 was not background-subtracted.

Notes on STEM-EELS spectra of Pt-SnO_2/C

Figure S8 shows elemental maps and EEL spectra from selected areas of Pt-SnO_2/C from a tin oxide-rich region to a platinum-rich region. Signals from the Sn $M_{4,5}$ edge (485 eV) and the O K edge (532 eV) are largely overlapping. The presence of O gives rise to two sharp peaks at ~550 eV. On Pt-dominant regions (area 5 in **Figure S8A, E** and the single particles in **Figure S4** and **Figure S5**) both Sn and O edges are absent, suggesting that oxygen atoms co-locate predominantly with Sn, not with Pt particles and the carbon support. In addition, even on regions where Pt, Sn and O are co-located (areas 2–4 in **Figure S8A, D**), the features of the O K edge are still clearly present and no obvious spectral differences can be found on these mixed regions compared to that of the tin oxide-rich region (area 1 in

Figure S8A, C). This observation seems representative of the majority of the regions analysed, as exemplified in **Figure S7**, highlighting similar features.

However, we note for completeness that for one cluster, metallic Sn was observed to be co-located with Pt nanoparticles that are in contact with SnO_2 (**Figure S9)**. This metallic Sn signal was evenly distributed across the nanoparticles (**Figure S10**), which indicates the formation of bulk alloyed Sn. The exact origin of the alloyed Sn is not clear, however, its detection does suggest the presence of alloyed Sn within in a small fraction of Pt-SnO_2 nanoclusters, at concentrations below the detection limit of XAS measurements (in air and in H_2). Further study would be necessary to clarify the stability of Pt-SnO_2 during STEM measurements and the origin of the alloyed Sn, however these are beyond the scope of the present work. Regardless of the origin and, based on the combined results presented in the main text and supporting information, it is reasonable to assume that the effect of any alloyed Sn is in practice minimal, when looking at the Pt-SnO_2/C sample as a whole.

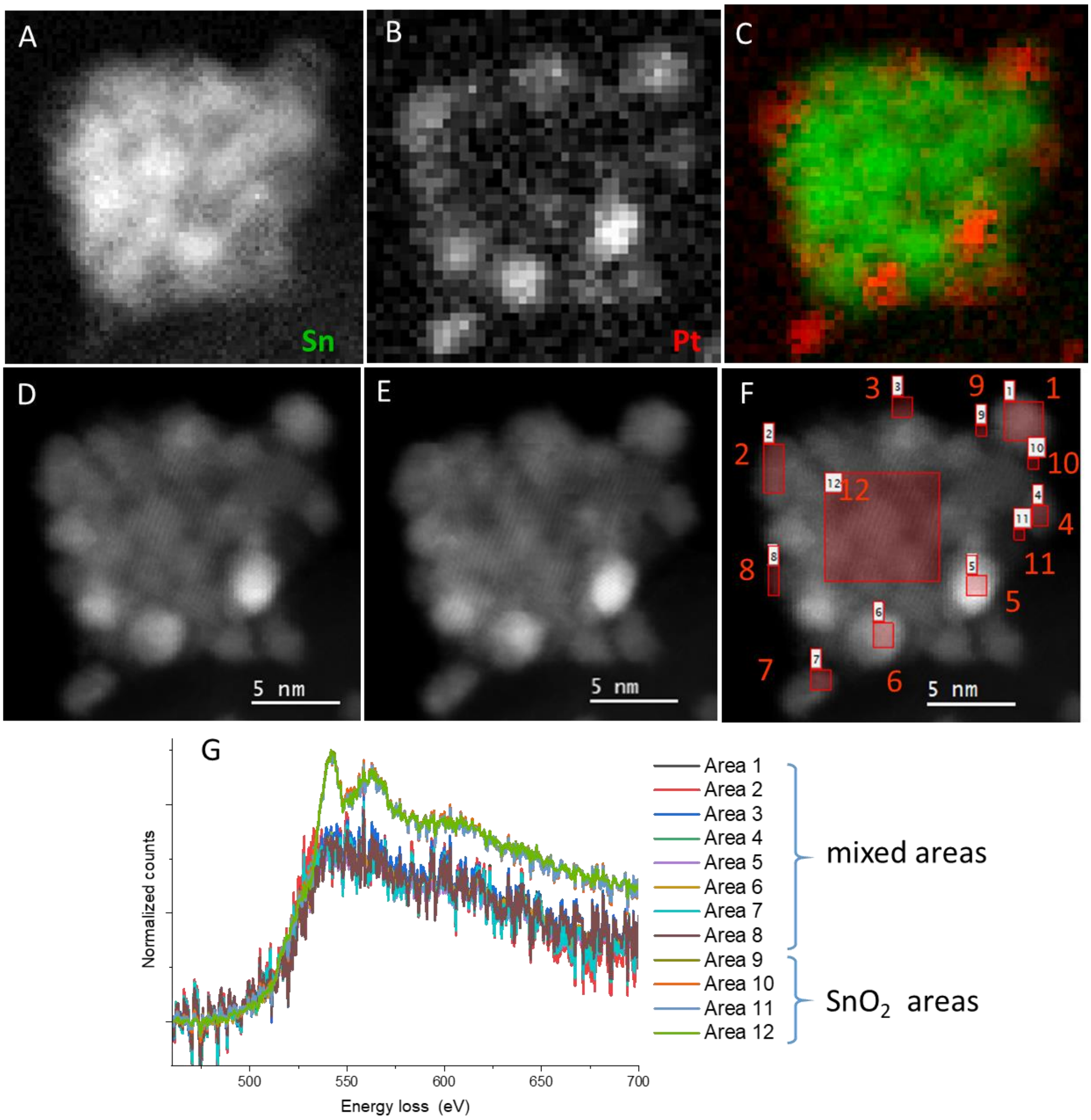

Figure S9 STEM-EELS analysis on a region that metallic Sn is present in all the Pt particles adjacent to SnO$_2$). Elemental mapping images of (A) Sn $M_{4,5}$ + O K, (B) Pt $M_{4,5}$ and (C) the overlapped, and (D and E) the corresponding HAADF images during mapping. (F and G) EELS spectra on the selected areas, showing the metallic Sn is present in all the Pt particles adjacent to SnO$_2$.

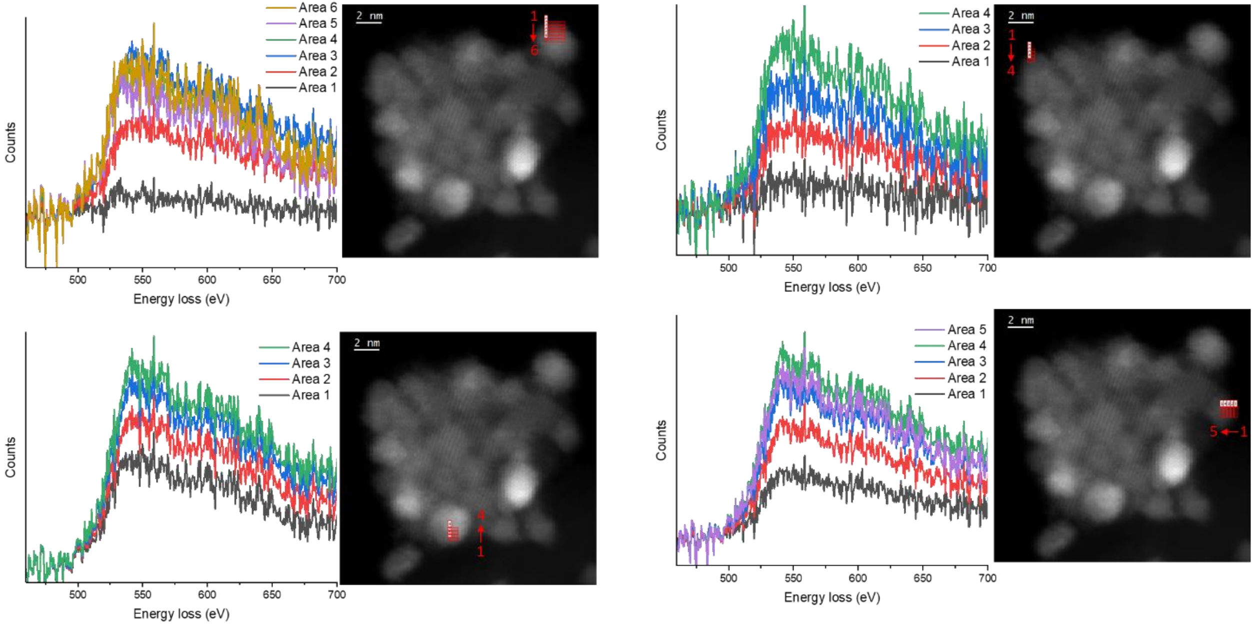

Figure S10 STEM-EELS analysis on four Pt nanoparticles in **Figure S9** with the selected area shown in the corresponding HAADF images on the right. The results show that the metallic Sn is not concentrated on the edge of the Pt nanoparticles, indicating that the metallic Sn was not limited to the surface of the Pt, possibly forming Pt-Sn alloys.

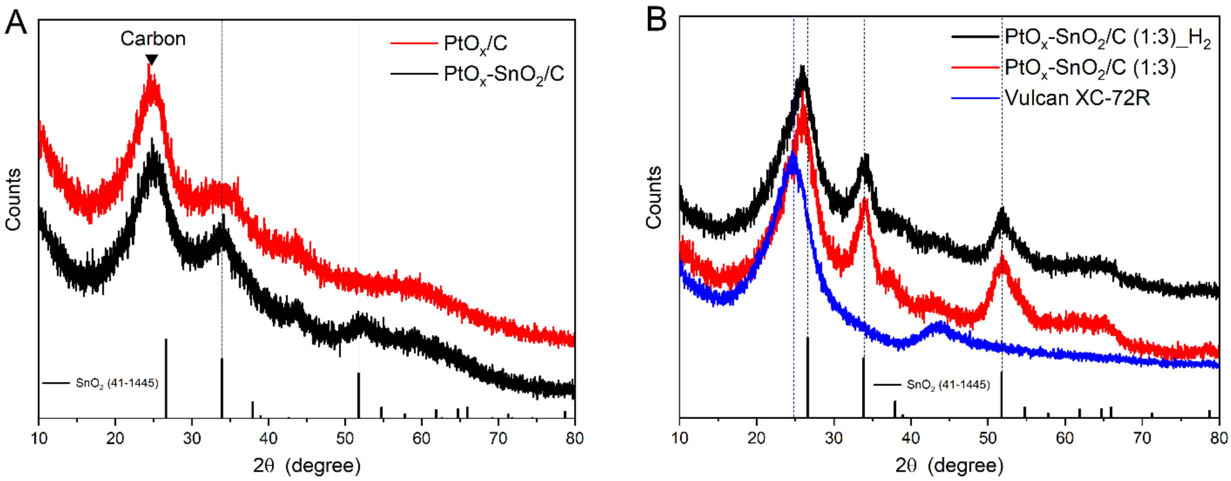

Figure S11. XRD patterns of (A) PtO_x/C and PtO_x-SnO_2/C with a nominal Pt-Sn molar ratio of 3:1 and (B) of 1:3, along with the standard peak positions of SnO_2 (JCPDS No. 41-1445) as vertical bars. The peaks ascribed to carbon support and SnO_2 is indicated by a blue line and three black dash lines, respectively.

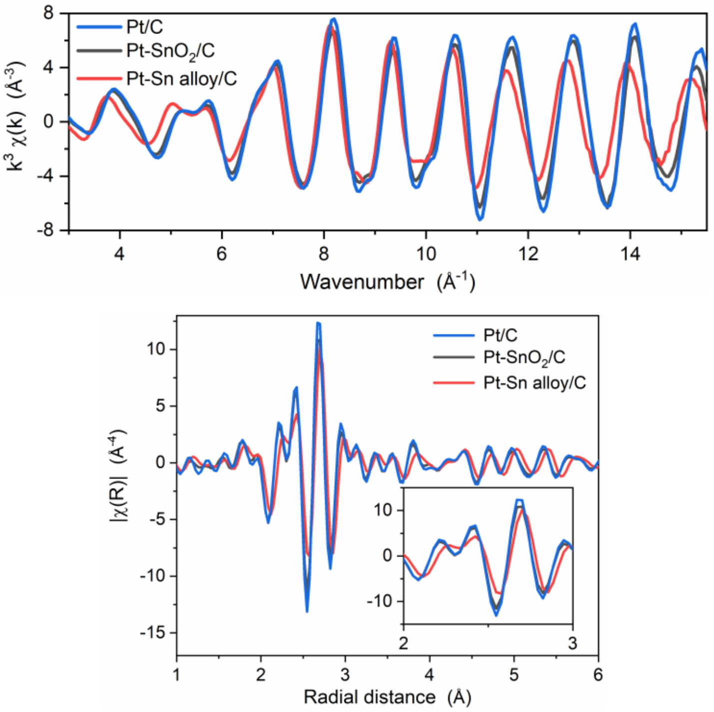

Figure S12. Same as **Figure 3A** but shown in (top) k space and (bottom) the real part of R space.

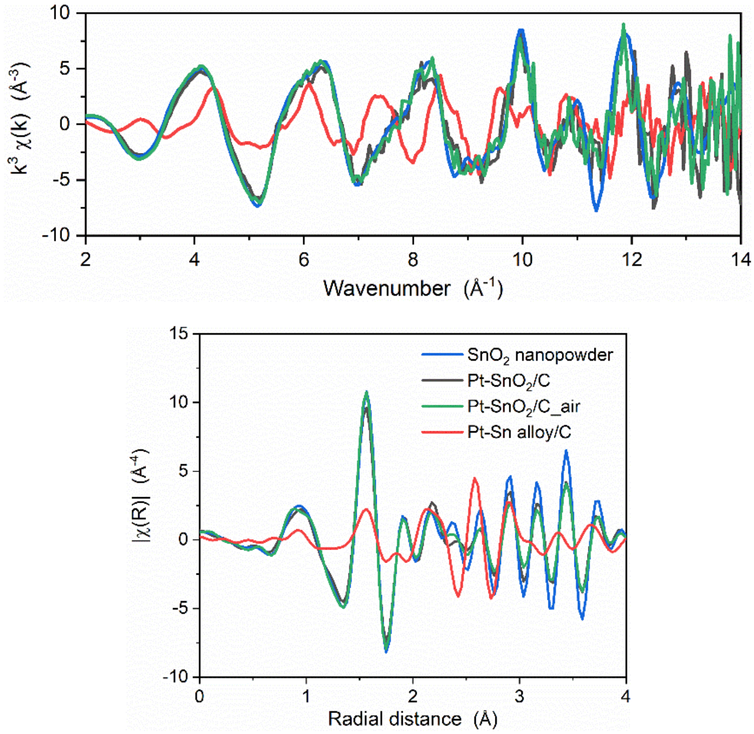

Figure S13. Same as **Figure 3B** but shown in (top) k space and (bottom) the real part of R space.

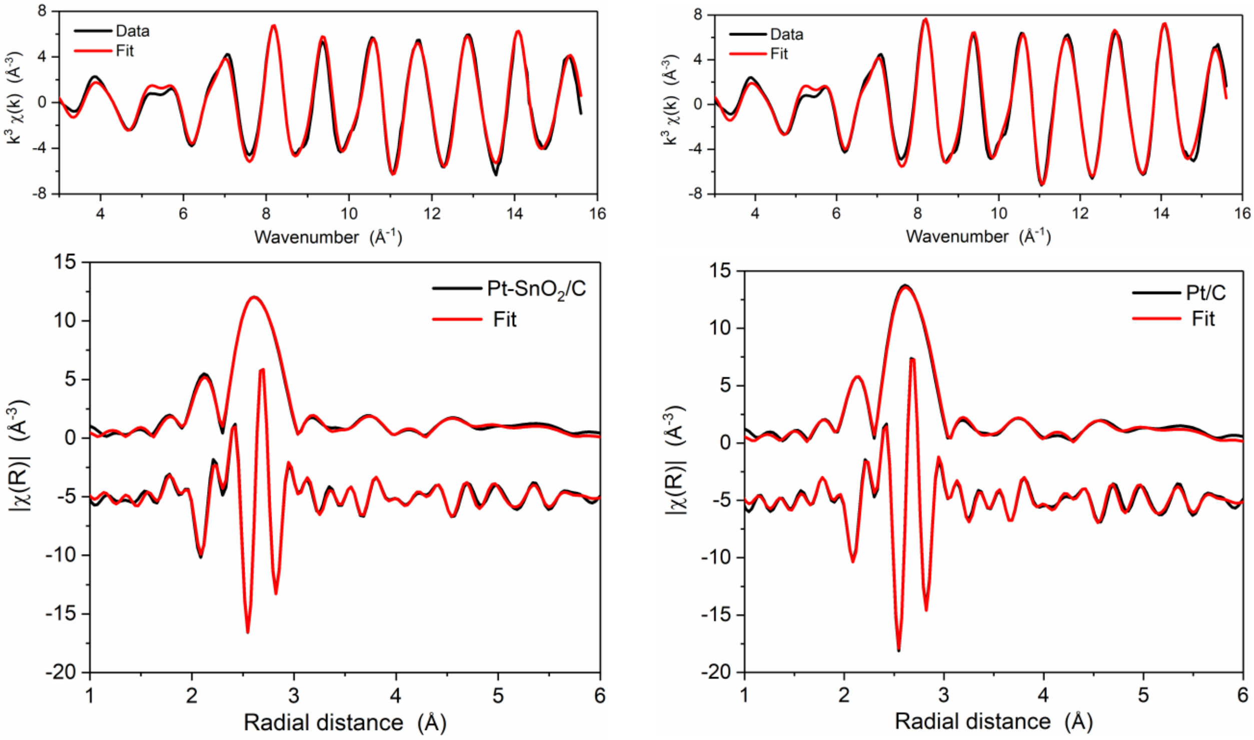

Figure S14. Fits of Pt L_3-edge EXAFS spectra (measured in H_2) of (left column) Pt-SnO_2/C and (right column) Pt/C, plotting as (top) k^3-weighted EXAFS spectra and (bottom) their Fourier transforms in magnitude and real part (offset by -5 Å^{-4} for clarity). The fitting was carried out in a R-range of 1.5 Å to 5.5 Å, producing R-factors of ~0.7% for Pt-SnO_2/C and ~0.6% for Pt/C. The structural parameters obtained are listed in **Table 1**.

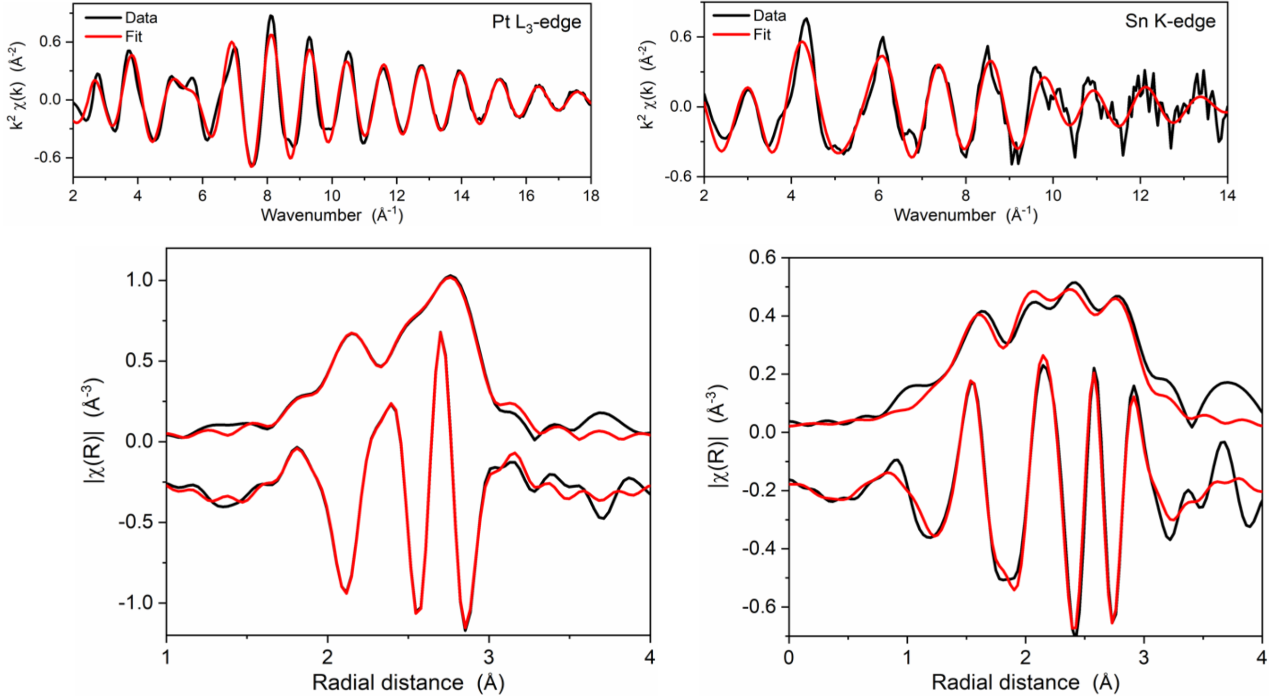

Figure S15. A first-shell fit of Pt-Sn alloy/C (measured in H_2) combining the data measured at the Pt L_3-edge (left column) and Sn K-edge (right column). (top) k^2-weighted EXAFS spectra and (bottom) their Fourier transforms plotted as magnitude and real part (offset for clarity by -0.3 Å^{-3} for Pt L_3-edge and -0.2 Å^{-3} for Sn K-edge). The combined fitting was carried out in R-ranges of 1.35–3.0 Å for Pt L_3-edge and of 1.0–3.0 Å for Sn K-edge, and produced a fit with a R-factor of 0.9% and structural parameters listed in **Table 1**.

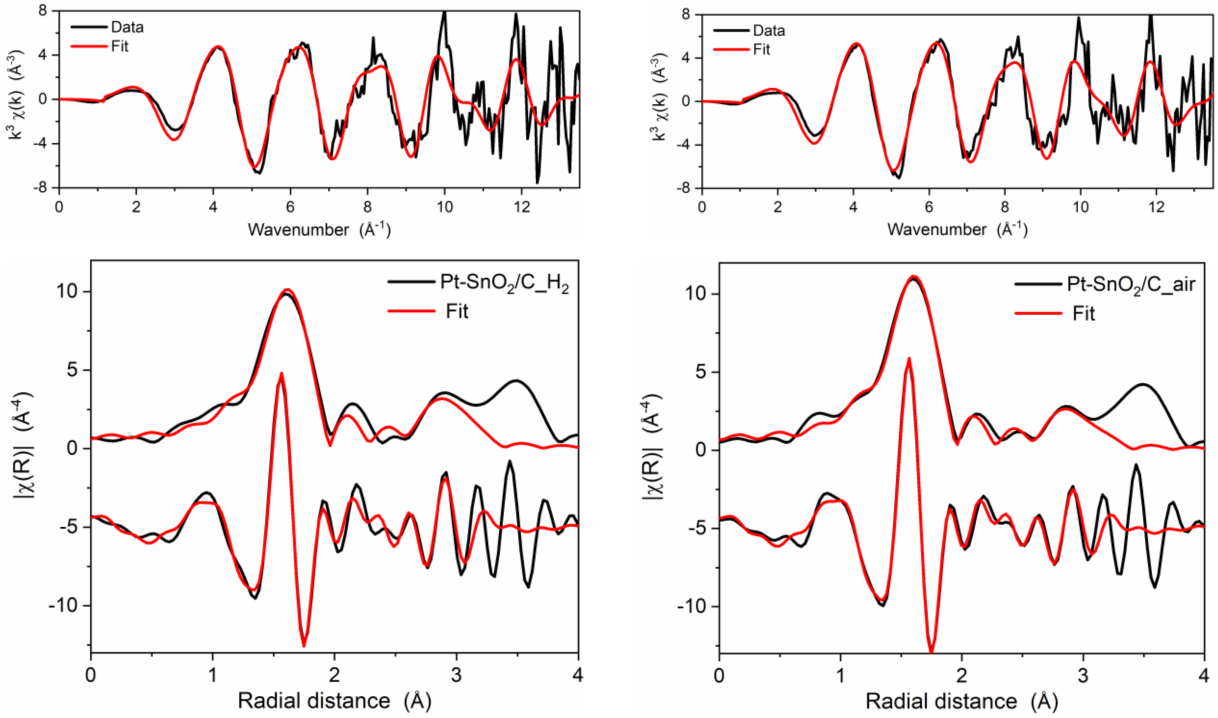

Figure S16. Fits of Sn K-edge EXAFS spectra of Pt-SnO_2/C measured in (left column) H_2 and (right column) air, plotting as (top) k^3-weighted EXAFS spectra and (bottom) their Fourier transforms in magnitude and real part (offset by -5 Å^{-4} for clarity). The fitting was conducted in 1.0–3.0 Å, producing R-factors of ~1.2% for that measured in H_2 and 0.4% for that in air. The structural parameters obtained are listed in **Table 1**.

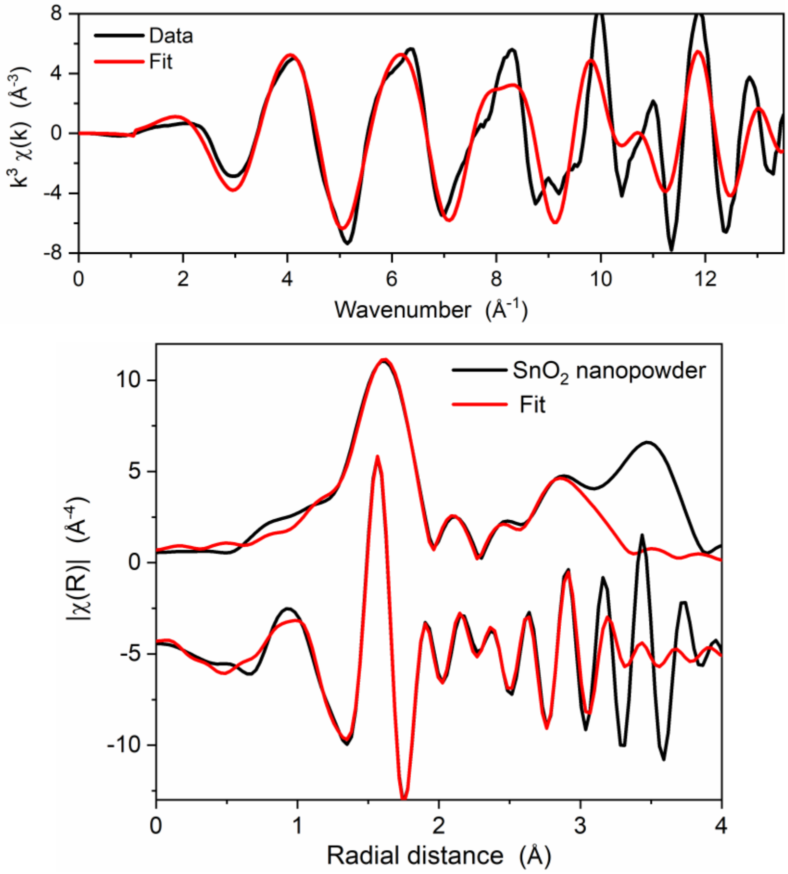

Figure S17. A fit of SnO_2 nanopowder (8–10 nm, Alfa Aesar) at Sn K-edge, plotting as (top) k^3-weighted EXAFS spectra and (bottom) their Fourier transforms in magnitude and real part (offset by -5 $Å^{-4}$ for clarity). The fitting was conducted in 1.0–3.0 Å, producing a R-factor of ~1.2%. The structural parameters obtained are listed in **Table 1**.

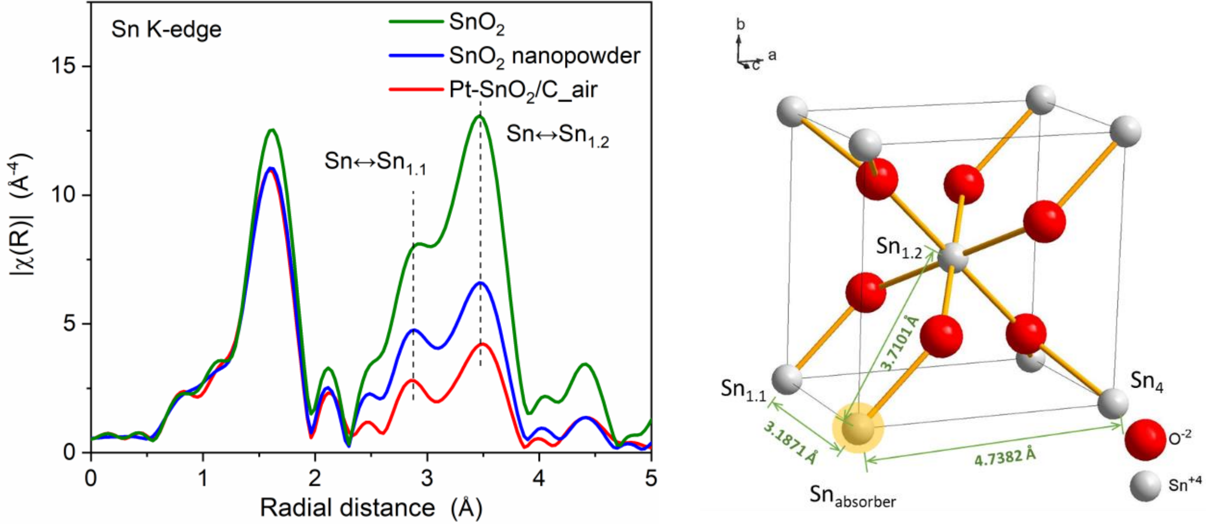

Figure S18. (Left) Fourier transforms of Sn K-edge EXAFS spectra of Pt-SnO_2/C (measured in air), SnO_2 nanopowder (8–10 nm, Alfa Aesar) and a SnO_2 reference sample, comparing the size effect of SnO_2 on the intensity of Sn–$Sn_{1.1}$ (R = 3.1871 Å) and Sn–$Sn_{1.2}$ single scattering paths (R = 3.7101 Å). (Right) The unit cell of rutile SnO_2 (ICSD No.647469), showing the corresponding Sn–Sn scattering paths in the crystal structure.

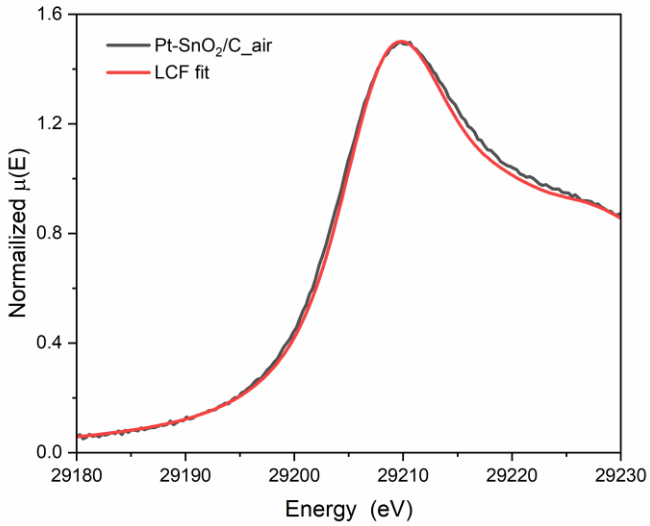

Figure S19 XANES linear combination fitting of Pt-SnO_2/C (measured in air) using SnO_2 and Pt-Sn alloy/C (measured in H_2) as the two references, yielding a R-factor (goodness of the fit) of 0.23%. The fitting result suggests that Pt-SnO_2/C is composed of (99.1±1.5)% SnO_2 and (0.9±1.5)% Pt-Sn alloy (containing some SnO_2). The fitting was carried in a window of 29184–29224 eV, 20 eV below and above the edge position.

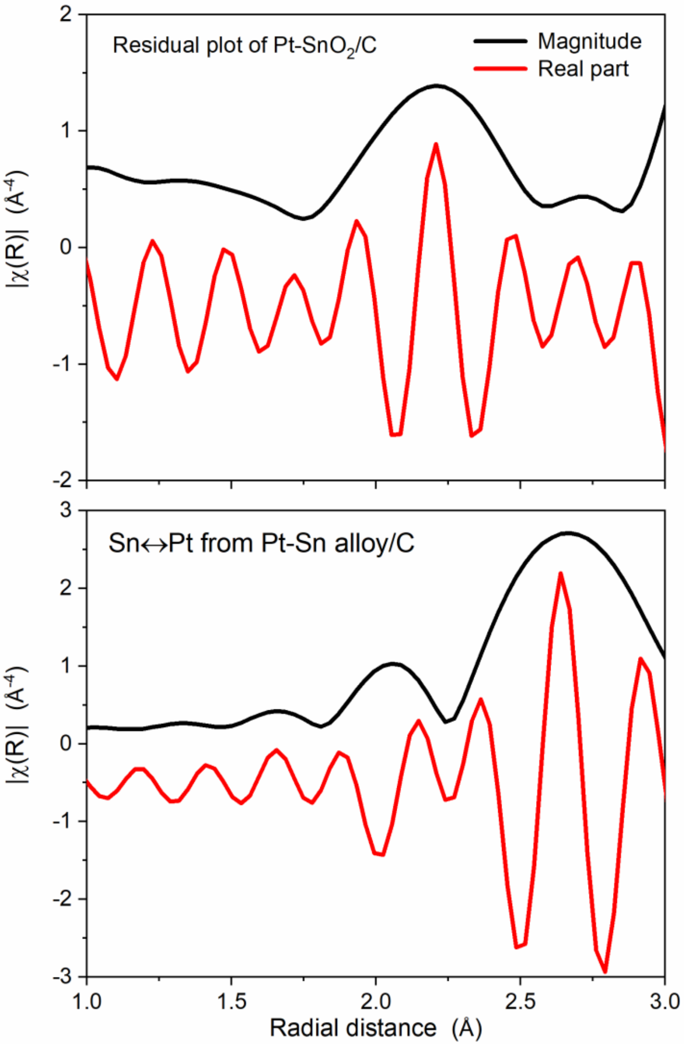

Figure S20. Comparison of (top) the residual plot from the fit of Pt-SnO$_2$/C (**Figure S16**) and (bottom) the Sn–Pt from the fit of Pt-Sn alloy/C (**Figure S15**) in the magnitude and the real part at Sn K-edge, showing that the mismatch between the Sn K-edge data of Pt-SnO$_2$/C and SnO$_2$ structural model is not in a close phase/position as the Sn–Pt of Pt-Sn alloy.

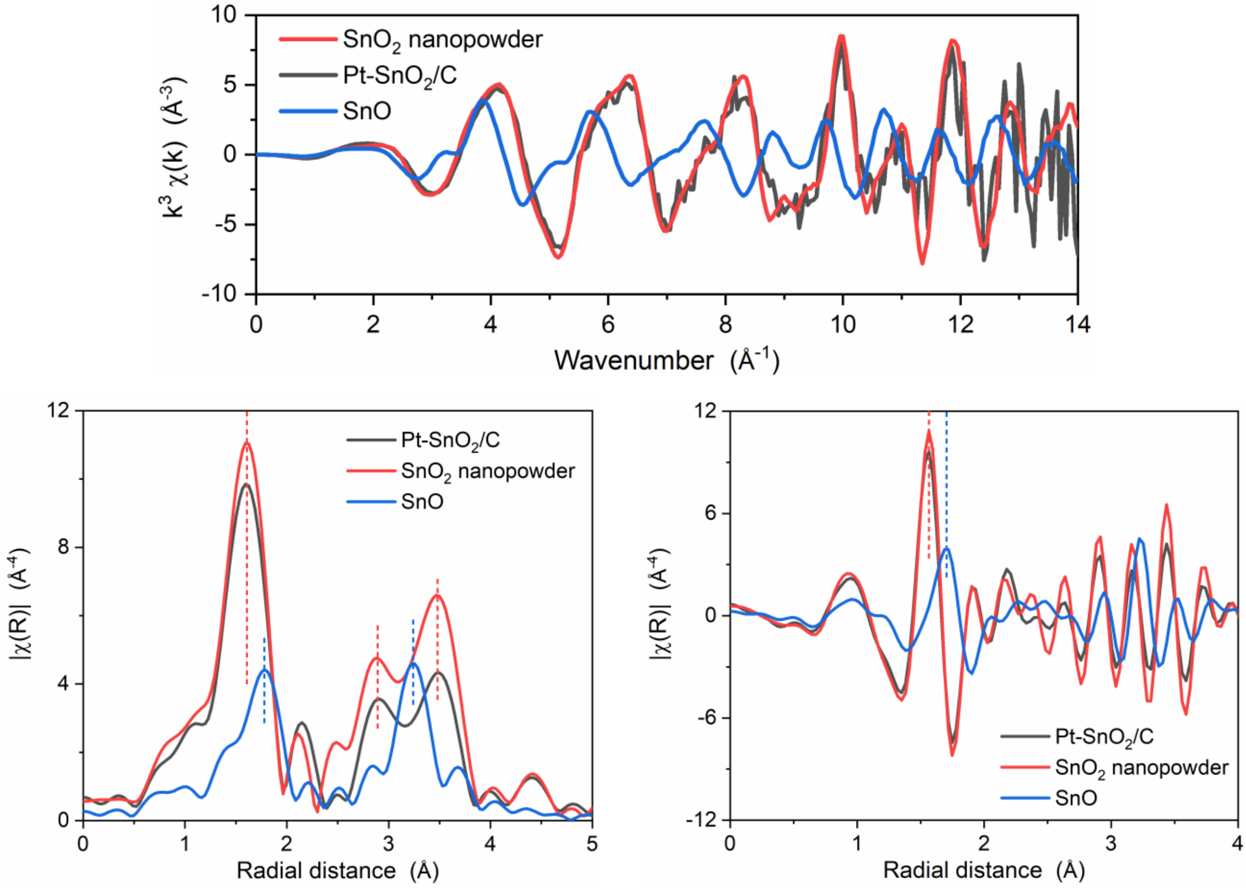

Figure S21. Comparison of the Sn K edge spectra of Pt-SnO_2/C, SnO_2 nanopowder and SnO in (top) k space, (bottom left) the magnitude of R space and (bottom right) the real part of R space, showing that the spectral features of Pt-SnO_2/C largely resemble those of SnO_2 nanopowder but are significantly different from those of SnO.

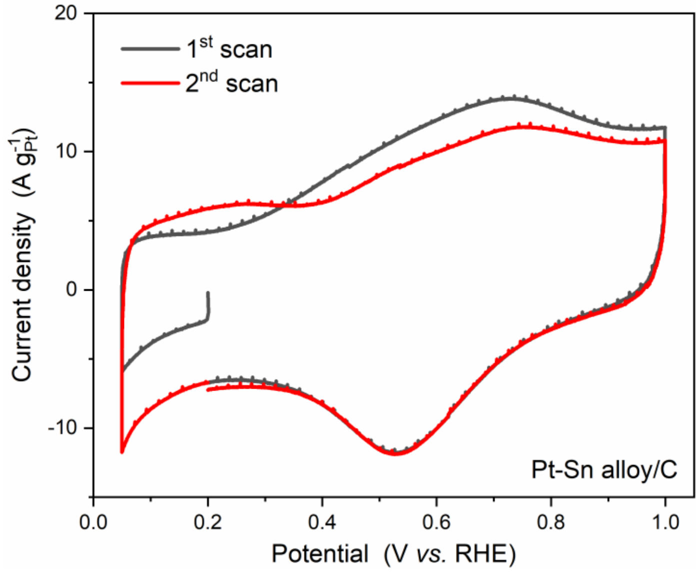

Figure S22. CO stripping voltammogram of Pt_3Sn alloy on carbon (20 wt% metal loading), with a scan rate of 20 mV s^{-1}.

Table S1. Electrochemical surface area (ECSA) of Pt estimated from CO-stripping voltammograms in **Figure 5** and **Figure S22**, assuming that a saturated CO- or H-adlayer on Pt is monolayer, and that the stripping of monolayer requires 210 μC cm_{Pt}^{-2} for H-adlayer and 420 μC cm_{Pt}^{-2} for CO-adlayer. A constant Y, extrapolated from the double layer capacitance region, was used as the baseline for integrating the charge gain from H adlayer desorption, and for CO-adlayer the difference between CO stripping voltammogram and the subsequent blank scan was used.

Samples	**ECSA-H (m^2 g_{Pt}^{-1})**	**ECSA-CO (m^2 g_{Pt}^{-1})**
Pt-SnO_2/C	76.6	111.7
Pt/C	86.0	109.7
Pt/C (20wt% JM)	75.2	106.1
Pt-Sn alloy/C	0.73*	1.3

*Due to the distorted voltammogram, the value was estimated using the same method for ECSA-CO

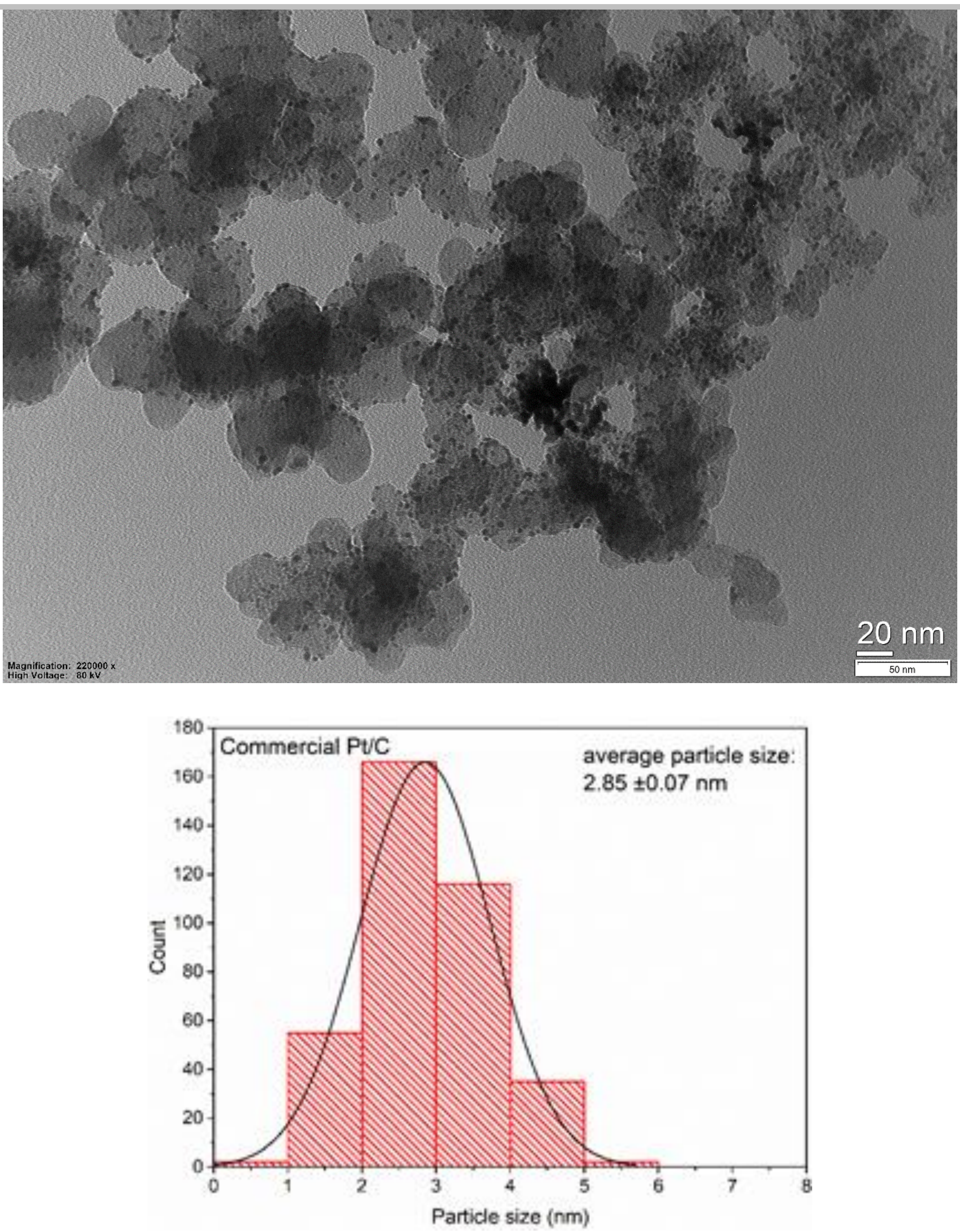

Figure S23. (A representative TEM image of the commercial Pt/C (20 wt%, JM), along with a histogram of particle size distribution.

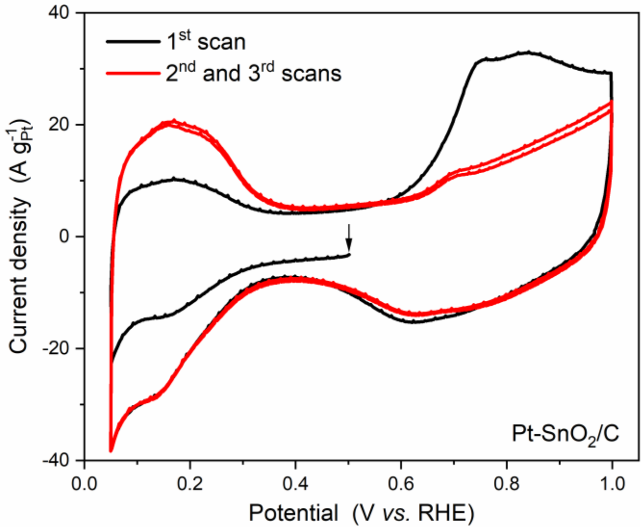

Figure S24. CO pre-stripping voltammogram on Pt-SnO$_2$/C in N$_2$-saturated 0.1 M HClO$_4$ with a scan rate of 20 mV s^{-1}. Before the voltammogram was measured, the saturated CO adlayer was partly stripped by potential hold at 0.5 V for 13 min in the solution. ~36% CO$_{ads}$ was removed on the basis of the charge difference in the H$_{des}$ waves between the 1st scan and the 2nd scan.

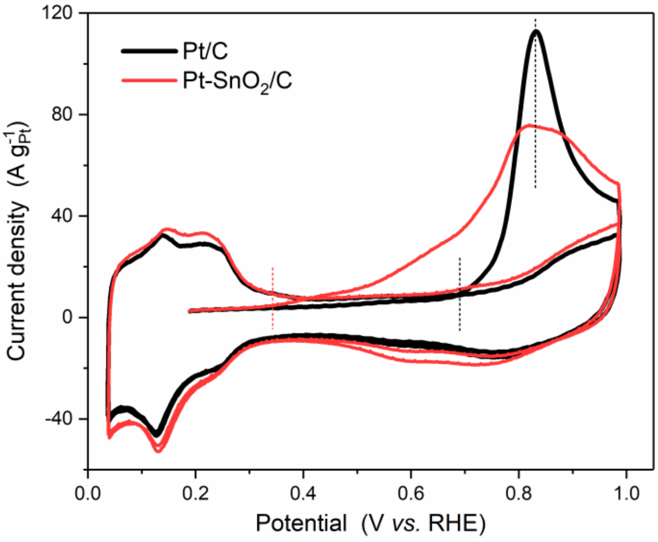

Figure S25. CO stripping voltammograms of Pt/C and Pt-SnO$_2$/C. The voltammograms were collected in N$_2$-saturated 0.1 M H$_2$SO$_4$ solution with a scan rate of 20 mV s^{-1}.

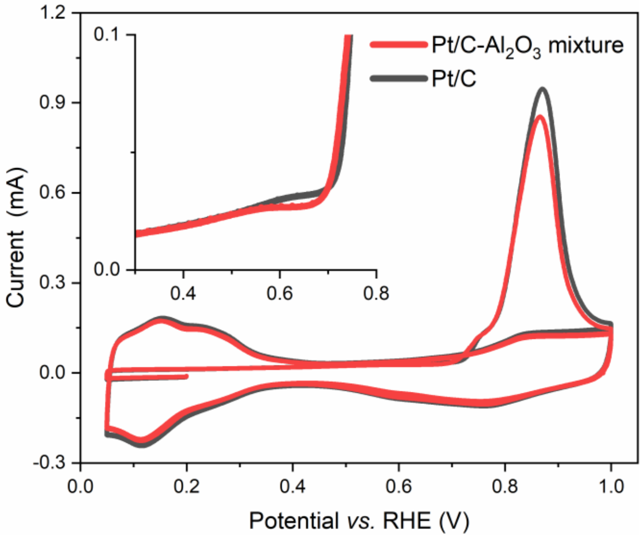

Figure S26. CO stripping voltammograms of a physical mixture of the Pt/C and Al_2O_3 (0.05 µm, MicroPolish Powder, BUEHLER). The voltammograms were conducted in N_2-saturated 0.1 M $HClO_4$ solution with a scan rate of 20 mV s^{-1}. The Al_2O_3 loading was ~46 µg cm^{-2} and the Pt loading was ~61 μg_{Pt} cm^{-2}. The inset magnifies the first sweeps of the voltammograms in the onset of CO_{ads} oxidation.

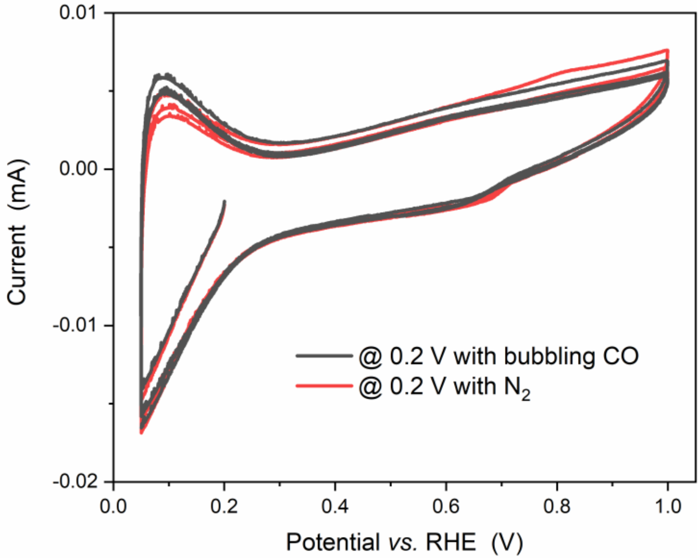

Figure S27. CO stripping voltammograms of SnO_2 nanopowders on a GC electrode, prior to which the electrodes were held at 0.2 V vs. RHE for 20 min with bubbling CO or with N_2, showing that SnO_2 is inert to CO adsorption and oxidation. The scan rate was 20 mV s^{-1}.

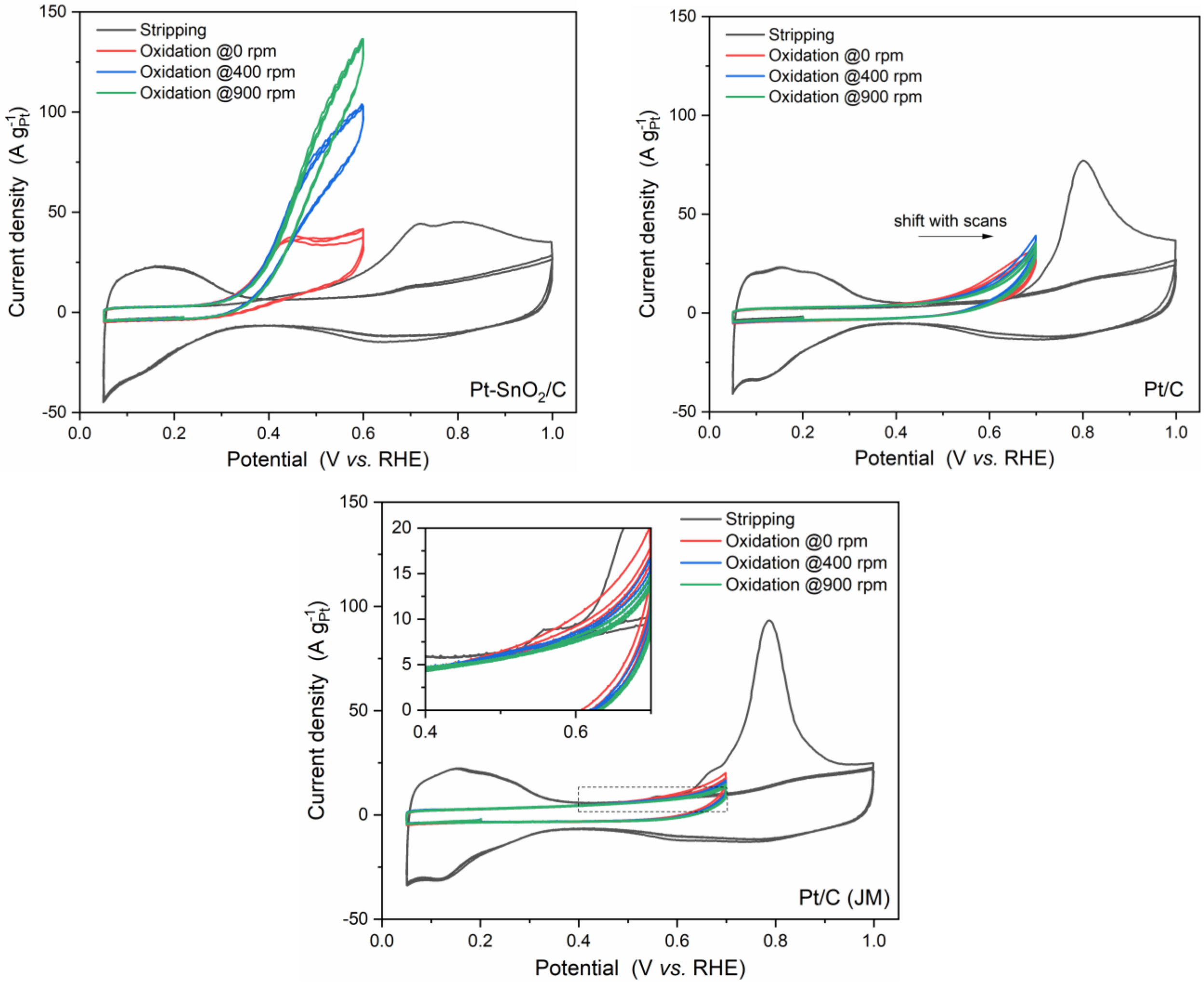

Figure S28. CO stripping and CO oxidation voltammograms of (top left) Pt-SnO$_2$/C, (top right) Pt/C and (bottom) Pt/C(JM) in 0.1 M HClO$_4$ with a scan rate of 20 mV s^{-1}. The cyclic voltammetry for CO oxidation was conducted in CO-saturated solution with different rotation rates (0 rpm, 400 rpm and 900 rpm in sequence), each of which was measured three scans. The prepared Pt/C yields a higher current than the commercial sample in continuous CO oxidation, which is the opposite to the CO stripping voltammograms. The opposite activity in CO oxidation activity can be attributed to the Pt particle size (~ 2 nm for the prepared and |3 nm for the commercial samples); the smaller particle size offers the higher fraction of defective sites, which facilitates the nucleation of Pt-OH$_{ads}$ at lower potentials[1], but decreases the lateral repulsion of Pt-CO$_{ads}$.

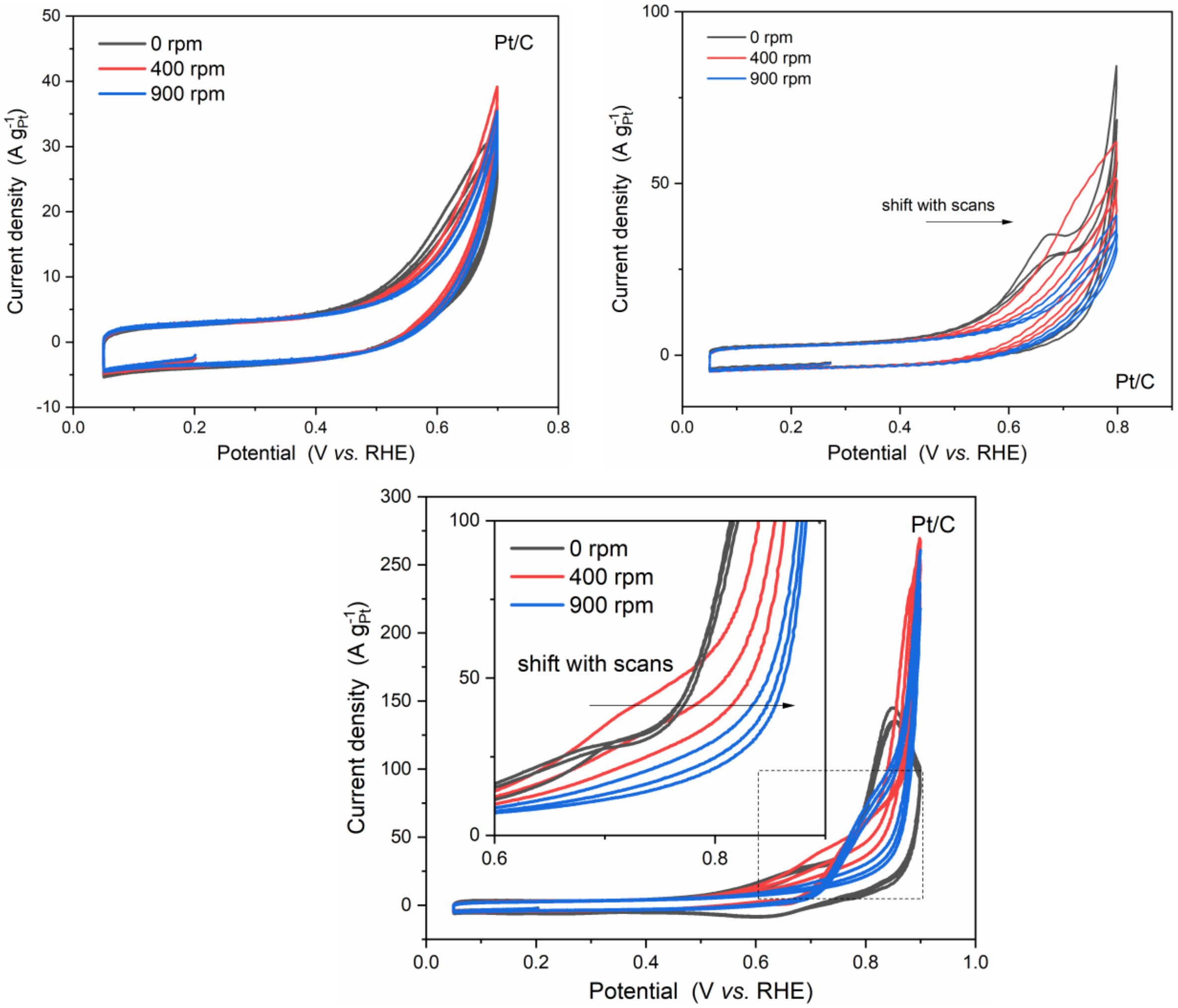

Figure S29. CO oxidation voltammograms of Pt/C in CO-saturated 0.1 M $HClO_4$ solution with upper potential limits of (top left) 0.7 V, (top right) 0.8 V and (bottom) 0.9 V. The rotation rates are indicated in the figure legends, and the inset of the right present only the forward scans of the magnified area, showing the oxidation waves shift positively with scans under convective-diffusion condition. The scan rates were 20 mV s^{-1}. The observed shift may, in part, be attributed to the effects of CO-annealing on the surface structure of the Pt nanoparticles and variations in the lateral repulsive interactions[2] between adsorbed CO molecules that accompany differences in the CO coverage during re-adsorption during the reverse sweep of the voltammogram.

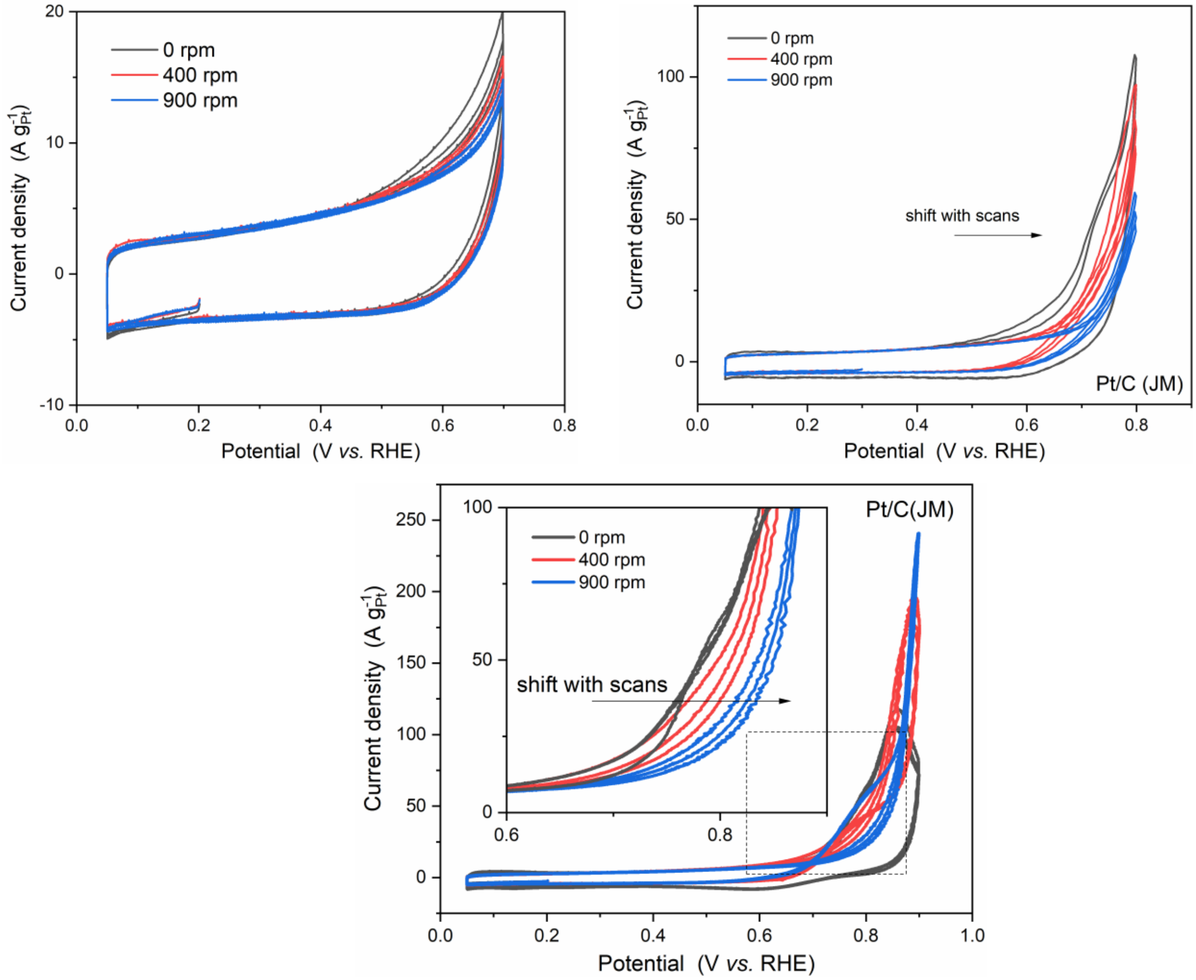

Figure S30. CO oxidation voltammograms of Pt/C (JM) in CO-saturated 0.1 M $HClO_4$ solution with upper potential limits of (top left) 0.7 V, (top right) 0.8 V and (bottom) 0.9 V. The rotation rates are indicated in the figure legend, and the inset of the right present only the forward scans of the magnified area, showing the oxidation waves shift positively with scans under convective-diffusion condition. The scan rates were 20 mV s^{-1}. As for the prepared Pt/C catalyst (Figure S29) the observed shift may be attributed in part to CO-annealing and/or variations in the CO coverage on re-adsorption.

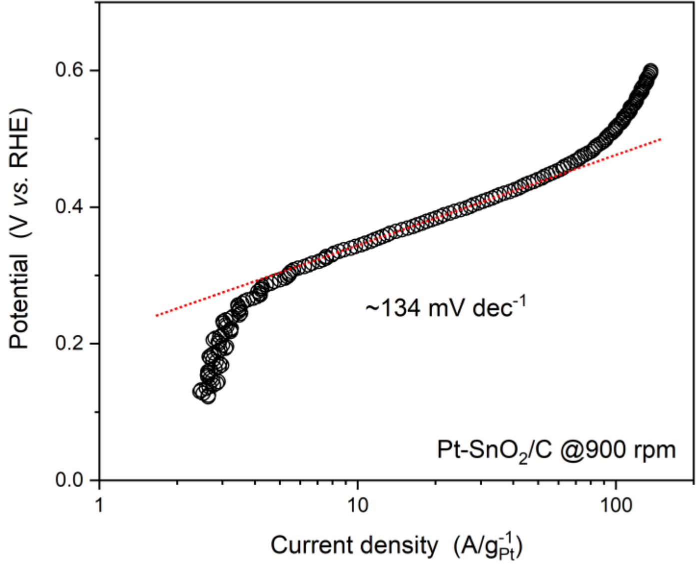

Figure S31. A Tafel plot of CO oxidation on Pt-SnO$_2$/C with 20 mV s^{-1} scan rate and 900 rpm rotation rate in CO-saturated 0.1 M HClO$_4$. The plot is not IR-corrected.

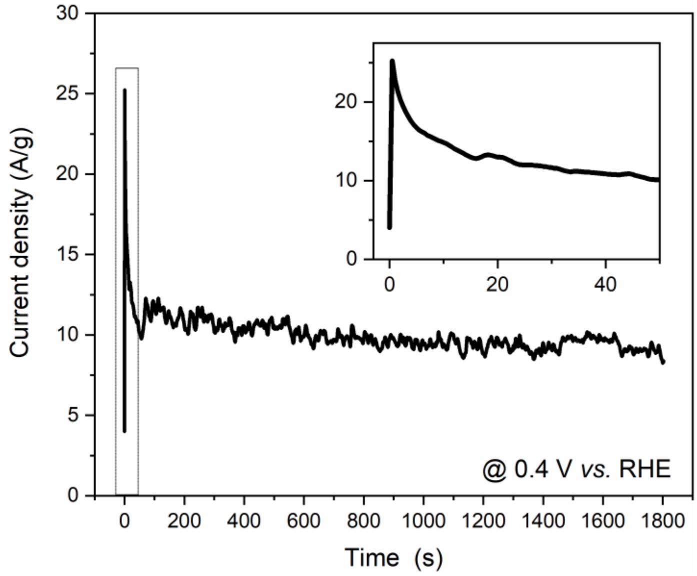

Figure S32. A 0.5 h chronoamperommogram of Pt-SnO$_2$/C for CO oxidation under an applied potential of 0.4 V *vs.* RHE and a rotation rate of 0 rpm in CO-bubbling 0.1 M HClO$_4$. The sharp decrease at the start is due to the contribution of capacitance current.

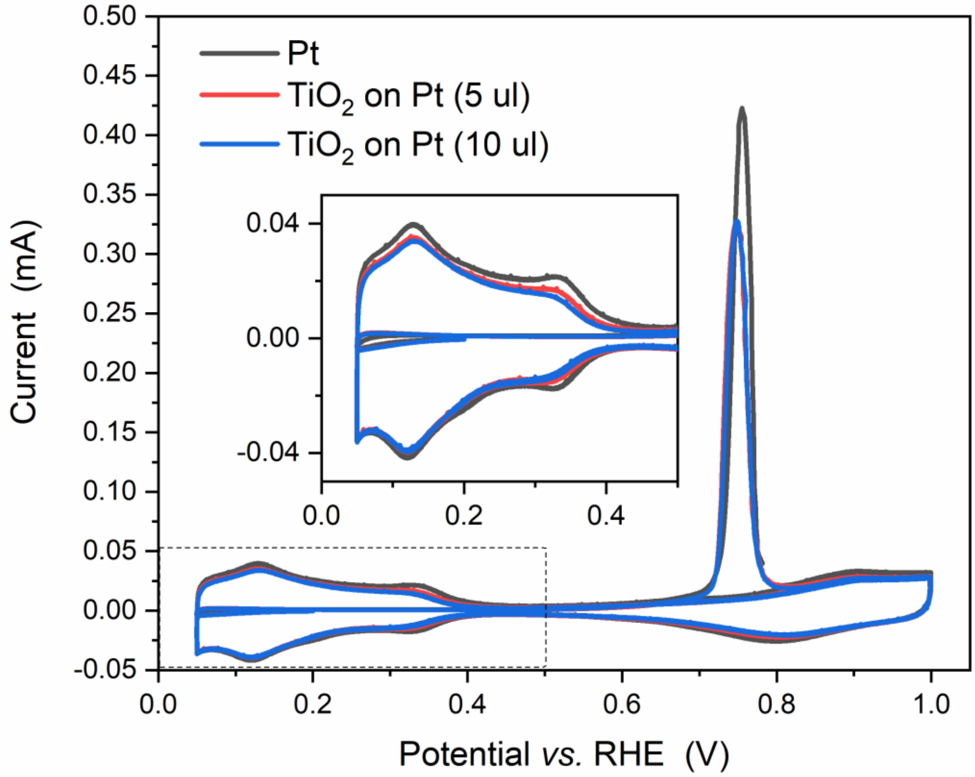

Figure S33. CO-stripping voltammograms of TiO_2-modified Pt electrode with three different loadings, 0, 5 and 10 ul 5 mg mL^{-1} TiO_2 suspension (H_2O-isopropanol solution with a water volume fraction of 60%) on a Pt electrode (5 mm diameter). The hydrogen region is magnified in the inset.

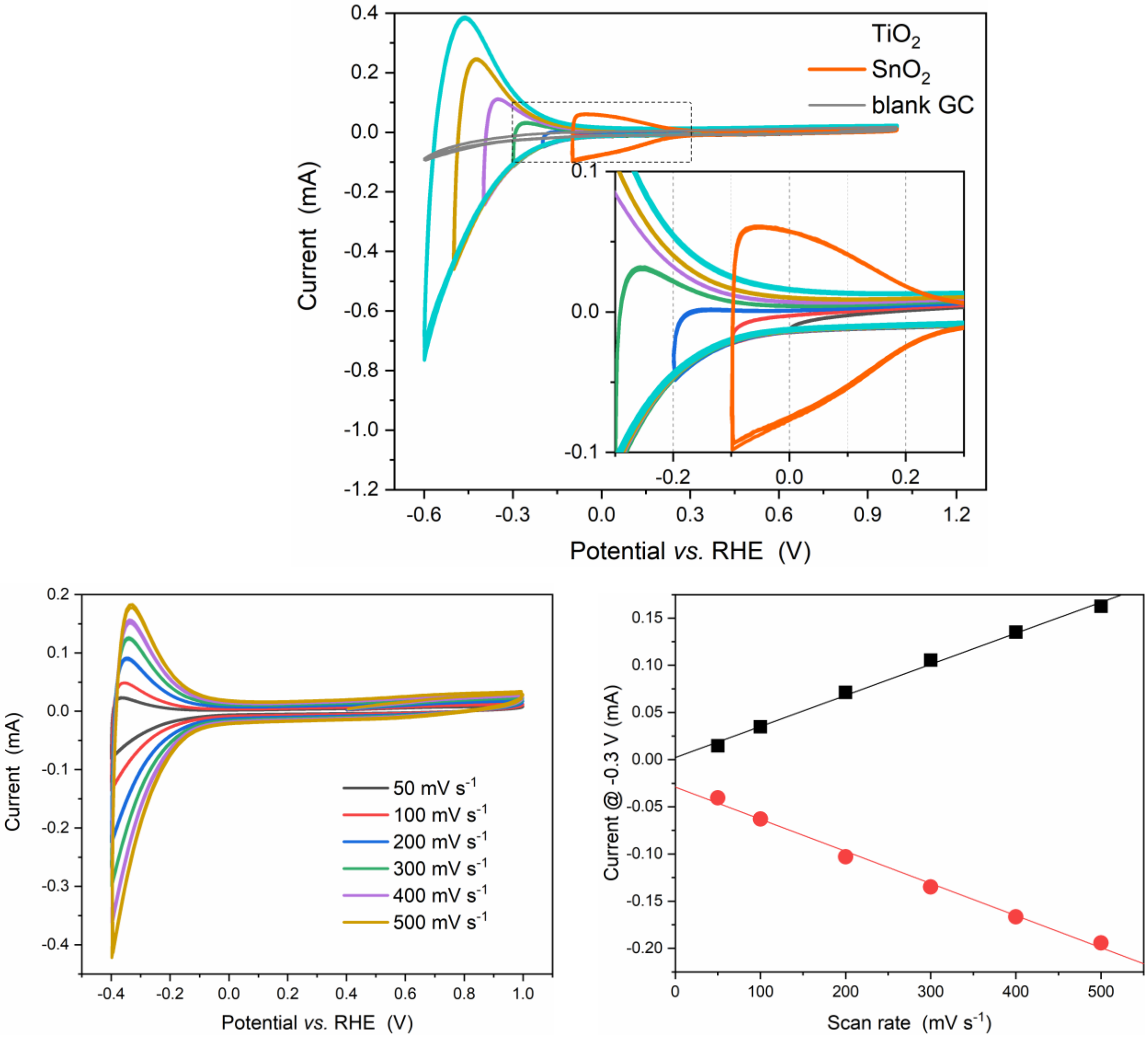

Figure S34. Cyclic voltammograms of TiO_2(P25) on a polished glassy carbon electrode (5 mm diameter) with (top) different potential lower limits (-0.6–0.0 V with an interval of 0.1 V) and (bottom left) different scan rates. (bottom right) The currents at -0.3 V were plotted against the scan rates, showing linear relationships between the anodic/cathodic currents and scan rates. In the window-opening experiment, the scan rate was 200 mV s^{-1}, and the SnO_2 data and the blank glassy carbon (GC) data with the same scan rate were compared.

References

[1] a) M. Arenz, K. J. Mayrhofer, V. Stamenkovic, B. B. Blizanac, T. Tomoyuki, P. N. Ross, N. M. Markovic, *J. Am. Chem. Soc.* **2005**, 127, 6819-6829; b) D. S. Strmcnik, D. V. Tripkovic, D. van der Vliet, K. C. Chang, V. Komanicky, H. You, G. Karapetrov, J. P. Greeley, V. R. Stamenkovic, N. M. Markovic, *J. Am. Chem. Soc.* **2008**, 130, 15332-15339.

[2] M.J.S. Farias, G.A. Camara, J.M. Feliu, *J. Phys. Chem. C.*, **2015**, 119, 20272-20282.